Research Article

Boyu Guo, Jincai Zhu*, Xiaokai Meng, and Qi Cao

Axial compression damage constitutive model and damage characteristics of fly ash/silica fume modified magnesium phosphate cement after being treated at different temperatures

https://doi.org/10.1515/rams-2024-0063 received July 10, 2024; accepted October 07, 2024

Abstract: The relationship between fly ash (FA) and silica fume (SF)-modified magnesium phosphate cement (MPC) at varying temperatures remains unclear. In this study, the mechanical properties and damage characteristics of FAand SF-modified MPC at 20-1,000°C were analysed through uniaxial compression tests. The results indicate that the compressive strength of MPC diminishes at varying temperatures, while FA and SF can enhance the compressive strength of MPC following exposure to high temperatures. In addition, with an increase in the temperature, the peak strain of MPC increased, and the deformation modulus first decreased and then increased. At 1,000°C, the deformation modulus of MPC was 5.09–10.92 GPa. The proposed damage constitutive model can predict the mechanical parameters of FA- and SF-modified MPC at different temperatures. The total damage variable reflects an "S-shaped" change trend under the action of axial compression loads. MPC exhibited irreversible initial temperature damage after being treated at different temperatures. More specifically, the temperature damage variable first increased and then decreased by increasing the temperature. At 600°C, the temperature damage variable exceeds 30% of the total damage variable associated with the peak strain, and at 1,000°C, it surpasses 10%.

Boyu Guo, **Qi Cao:** School of Civil Engineering, Inner Mongolia University of Technology, Inner Mongolia, Hohhot, 010051, China; School of Architectural Engineering, Hulunbuir University, Inner Mongolia, Hulun Buir, 021008, China

Xiaokai Meng: College of Science, Inner Mongolia University of Technology, Inner Mongolia, Hohhot, 010051, China

Keywords: magnesium phosphate cement, temperature effect, fly ash and silica fume, damage constitutive model, damage variable

1 Introduction

Fire is undoubtedly a severe challenge building structures face [1]. In high-temperature environments, building materials experience changes in their chemical composition and mechanical properties, which could result in structural failure [2-4]. Magnesium phosphate cement (MPC) is formed through the acid-base neutralization reaction of dead burned magnesia (MgO) and soluble phosphates in contact with water. The main hydration product is an amorphous magnesium phosphate complex, MgKPO₄·6H₂O/ MgNH₄PO₄·6H₂O (struvite), which is the MPC system that produces the root of the gelling properties [5-8]. The respective hydration process is shown in Eqs. (1) and (2). In comparison to ordinary Portland cement, MPC possesses the comparative advantages of fast hardening, early strength [9,10], good environmental adaptability [5], good volume stability [11], and good bonding performance with old concrete [12]. It is mainly used in the fields of rapid repair [13], biomedical engineering [14], solidification of heavy metals, and radioactive waste [15].

$$MgO + KH_2PO_4 + 5H_2O \rightarrow MgKPO_4 \cdot 6H_2O(K-struvite),$$
 (1)

$$MgO + NH2H2PO4 + 5H2O \rightarrow MgNH4PO4$$

$$\cdot 6H2O(struvite),$$
(2)

Fly ash (FA) and silica fume (SF) are two prevalent industrial by-products that are often integrated into cement concrete as supplementary cementing materials to lower CO₂ emissions [16,17], decrease energy consumption [18], and enhance the performance of cement concrete [16,19–22]. To improve the performance of MPC, as well as

^{*} Corresponding author: Jincai Zhu, School of Civil Engineering, Inner Mongolia University of Technology, Inner Mongolia, Hohhot, 010051, China; Key Laboratory of Civil Engineering Structure and Mechanics, Inner Mongolia Autonomous Region, Inner Mongolia, Hohhot, 010051, China, e-mail: jczhu@imut.edu.cn

to reduce the preparation cost, FA, SF, and other admixtures are usually incorporated during the preparation process [16,17]. FA and SF can reduce the exothermic heat of hydration, improve the compressive strength, and optimize the pore structure when incorporated into MPC [18-21]. At the same time, SiO₂ in FA and SF participates in the hydration reaction of MPC to form MgSiO3 gel, thus improving the micro-morphology of MPC and filling the cracks and pores of the matrix [23]. In recent years, with the application of MPC in high-temperature environments as a refractory material and steel fireproof coating [24,25], its high-temperature resistance has attracted the attention of the scientific community. Li et al. [26] found that high temperatures led to dehydration of the hydration products of MPC, decreased the compressive strength, and increased the mass loss by placing the MPC at 130, 500, and 1,000°C. Dai et al. [27] found that borax reacted with MgO to form magnesium borate (Mg₃B₂O₆) at about 800°C. The authors reported that when the temperature was higher than 900°C, Mg₃B₂O₆ formed a liquid phase to fill the pores, which reduced the porosity of MPC and improved the compactness of MPC after being treated at high temperatures. Moreover, the compressive strength of the MPC doped with 15% borax at 1,100°C reached 95.2 MPa, which was three times higher than that of the MPC doped with 3% borax. Gardner et al. [28] measured the performance of MPC doped with FA and slag (GBFS) at 400-1,200°C, pointing out that MPC mixed with FA and GBFS did not exhibit peeling or cracking and had good volume stability. At the temperature value of 400°C, MgKPO₄·6H₂O dehydrated to MgKPO₄; and at the temperature range from 1,000 to 1,200°C, magnesium olivine (Mg₂SiO₄), spinel (MgAl₂O₄), leucite (KAlSi₂O₆), and other phases were generated. Zhang et al. [29] found that MPC mixed with calcium aluminate cement produced MgAl₂O₄ at high temperatures, with a denser microstructure and increased compressive strength. Fang et al. [30] utilized MPC as a flame-retardant coating and found that MPC absorbs some heat after dehydration of hydration products at high temperatures, which plays a role in delaying the spread of fire. It has also been reported in the literature that the incorporation of active oxides, such as Al₂O₃ and SiO₂ can improve the high-temperature resistance of MPC [31].

From the abovementioned analysis, it can be inferred that the research on the high-temperature resistance of MPC mainly focuses on the basic mechanical properties and microstructure. However, the constitutive relationship between FA- and SF-modified MPC after the application of various treatment procedures at different temperatures has been seldom examined. Nevertheless, the latter is considered of great importance for structural design and analysis. Therefore, to further study the basic mechanical properties and stress-strain relationship of MPC after being treated at different temperatures, uniaxial compression tests on FA- and SF-modified MPC at various temperatures were conducted in this work. Based on damage mechanics theory and the principle of equivalent stress, combined with the stress-strain curve, the axial compression damage constitutive model of FA- and SF-modified MPC after action at different temperatures. The impact of temperature on the compressive strength, peak strain, and deformation modulus of MPC were also analysed. The damage evolution law of MPC under axial compression load after action at different temperatures was thoroughly investigated. Our work provides a theoretical basis for the evaluation of the bearing performance of MPC under such conditions.

2 Raw materials and test methods

2.1 Raw materials

The MPC used herein was composed of magnesium oxide (MgO, M), potassium dihydrogen phosphate (KH₂PO₄, P), borax (Na₂B₄O₇·10H₂O, Br), FA, and SF in a certain proportion. Table 1 lists the oxide content of MgO, FA, and SF. Figure 1 shows the particle size distribution of MgO, FA, and SF, with an average particle size of 96.88, 86.76, and 13.74 μ m, respectively.

2.2 Mix design

The MPC mix ratio is listed in Table 2. M/P was in a molar ratio of 6:1, the borax (Br) content was 0.09 (Br/M) of the

Table 1: Oxide composition of the used raw materials

Oxide composition	MgO	SiO ₂	Al ₂ O ₃	CaO	Fe ₂ O ₃	Na ₂ O	K ₂ O	Others
MgO (%)	86.96	6.29	0.07	1.22	0.60	2.64	0.63	1.59
FA (%)	2.77	48.08	22.70	15.17	4.45	2.01	1.53	3.29
SF (%)	_	92.72	3.41	0.26	_	0.72	0.83	2.06

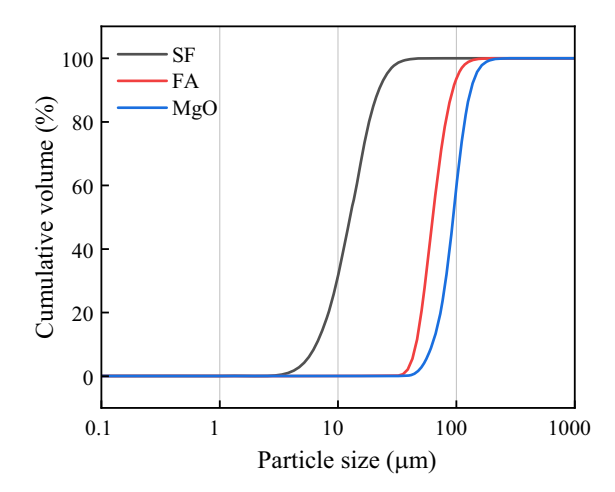


Figure 1: Particle size distribution of the raw materials.

Table 2: MPC mix proportion

Specimen types	M/P	Міх рі	W/B	Br/M		
		M + P	SF	FA		
M0	6:1	100	0	0	0.16	0.09
F1	6:1	90	0	10	0.16	0.09
F2	6:1	80	0	20	0.16	0.09
F3	6:1	70	0	30	0.16	0.09
F4	6:1	60	0	40	0.16	0.09
S1	6:1	95	5	0	0.16	0.09
S2	6:1	90	10	0	0.16	0.09
S3	6:1	85	15	0	0.16	0.09
S4	6:1	80	20	0	0.16	0.09
C1	61	90	5	5	0.16	0.09
C2	6:1	80	10	10	0.16	0.09

Note: $B = MgO + KH_2PO_4 + FA/SF/(FA+SF)$.

total mass of MgO, and the water-binder ratio W/B was 0.16. The FA/(M + P) was 10, 20, 30, and 40%, and due to the low density of SF, it was extremely difficult to form the SF doping greater than 20% during the preparation process; therefore, the SF/(M + P) was 5, 10, 15, and 20%, respectively. FA + SF/(M + P) was 10 and 20%, respectively, and FA + SF was 5% + 5% and 10% + 10%, respectively.

2.3 Specimen preparation

The size of the MPC specimen was $40 \, \text{mm} \times 40 \, \text{mm} \times 40 \, \text{mm}$. The following preparation process was applied: first, the weighed MgO, KH₂PO₄, Br, FA, and SF were put into the stirring pot and slowly stirred for 1 min to ensure even dispersion; next the mixture was slowly stirred with water for 30 s, and then quickly stirred for 1 min; the MPC

slurry was poured into the mould and put on the vibration table. After the surface of the specimen was free from obvious bubbles, the excess slurry was scraped off and compacted using a scraper. After 1h, the mould was removed, and the specimens were placed in a room at a temperature of $(20 \pm 2)^{\circ}$ C and a relative humidity of $(50 \pm 5)\%$ for 28 days.

2.4 Temperature rise system

The heating process is depicted in Figure 2. Under the temperature action, part of the water in the specimen was evaporated to avoid the water vapour gathering in the closed furnace and failing to volatilize, which could lead to the explosion of the furnace due to the high moisture content. The MPC specimen that was subjected to natural curing for 28 days was placed in an oven at 105°C for 24 h; then, the specimen was taken out and placed in a room for 6 h. The specimen was placed in the crucible frame and, finally, in the muffle furnace for high-temperature testing. The heating rate is 10°C·min⁻¹, and the specimen was heated to 200, 400, 600, 800, and 1,000°C for 3 h. After 3 h, the specimens were removed and placed in an indoor environment for 24 h; finally, uniaxial compression tests were carried out.

2.5 Uniaxial compression test

The MTS servo-hydraulic loading system loaded with the MPC specimens were subjected to high temperatures. The

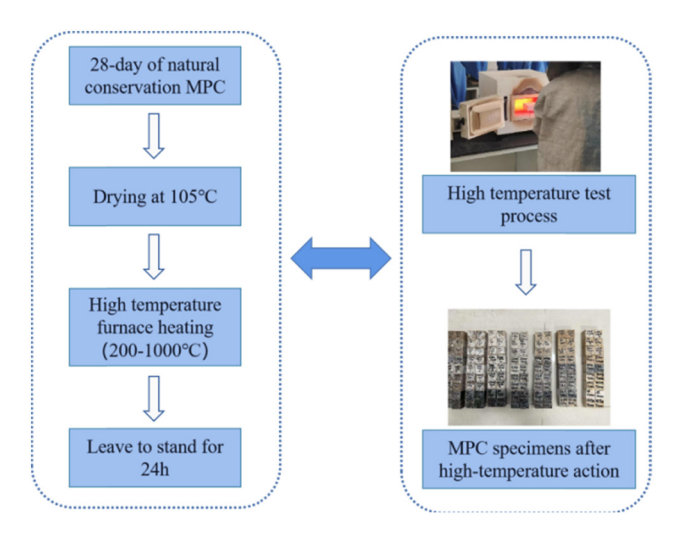


Figure 2: Flow chart of the high-temperature tests.

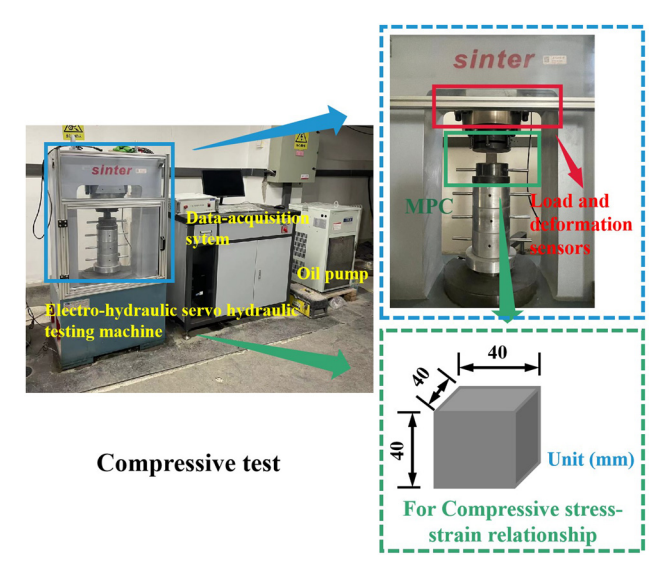


Figure 3: Flow chart of the uniaxial compression test.

loading mode was controlled by force, and the loading rate was set at $0.5 \, \mathrm{kN \cdot s^{-1}}$. The loading system's sensor measured the load and deformation, and the deformation accuracy was ±1%, as displayed in Figure 3. Preloading was performed before each load, and the data were collected when stress and strain were increased in direct proportion.

3 Experimental results and discussion

3.1 Apparent characteristics

The apparent characteristics of the MPC specimens after action at different temperatures are illustrated in Figure 4. As can be seen, MPC can still maintain good volume integrity after being treated at different temperatures, and no burst phenomenon occurred in the high-temperature test. The apparent colours of M0 and F2 under natural curing were reddish brown and light yellow, respectively. Additionally, a small difference in the apparent characteristics of the specimens after action at different temperatures was detected, with only a tiny number of micro-cracks being generated on the surface of M0. Both S4 and C2 were black under natural curing, and the apparent change in the specimen was not evident at temperatures below 600°C. When the temperature exceeded the value of 800°C, the S4 specimen gradually changed to greyish-white and exhibited obvious penetrating cracks; the cracking phenomenon of the C2 specimen was less than that of S4.

3.2 Compressive strength

Figure 5 displays the compressive strength of MPC after being treated at different temperatures. As can be observed, when the temperature was 20°C, the compressive strength of MPC was between 29.83 and 50.81 MPa. Moreover, the incorporation of FA and SF improved the compressive strength of MPC, among them, the compressive strength of S2 was the largest, at 50.81 MPa, which was 70.3% higher than that of M0. The maximum compressive strength of F2 in MPC containing FA was 39.32 MPa, which was 31.8% higher than that of M0. For MPC with co-doped FA and SF, the compressive strength of C1 was the largest, at 45.09 MPa, which was 51.2% higher than that of M0. The reasons for the improvement in the compressive strength of MPC by FA and SF are as follows: (i) The particle size of FA and SF is relatively small, which can improve the pore structure and micro-cracks of MPC by filling and improving the compactness of MPC specimens [32]. (ii) The active oxides, such as Al₂O₃ and SiO₂, in FA and SF will react with the unreacted MgO and KH₂PO₄ in MPC to form KAlSi₂O₆ and MgSiO₃. The latter material configurations have good chemical compatibility with struvite and contribute to the formation of an interconnected microstructure [23,33,34]. Furthermore, at different temperatures, the compressive strength of MPC decreased. At 105°C, the compressive strength of MPC decreased the most. The decrease was between 22 and 45.4%, which was attributed to the evaporation of free water inside MPC and the shedding of MgKPO₄·6H₂O bound water at 105°C, leading to an increase in the number of pores inside the specimen and the internal defects [29,35]. In the temperature range of 200-600°C, the compressive strength of MPC still continued to decrease, but the decrease in amplitude was reduced. At 600°C, the minimum compressive strength of M0 was 11.58 MPa, which was 38.8% of the strength of the natural curing; the compressive strengths of F1–F4 were 12.54, 13.15, 12.36, and 12.75 MPa, respectively, which were 8.3, 13.6, 6.7, and 10.1% higher than those of M0; and the compressive strengths of S1-S4 were 16.38, 17.83, 20.24, and 16.98 MPa, respectively, which were 41.5, 54.0, 74.8, and 46.6% higher than those of M0; and the compressive strengths of C1 and C2 were 18.16 and 18.41 MPa, respectively, which were 56.8 and 59.0% higher than that of M0, respectively. When the temperature was 1,000°C, the compressive strength of MPC increased to a certain extent. The compressive strengths of F1–F4 were 20.79, 22.47, 21.18, and 17.91 MPa, respectively, which were 37.6, 48.7, 40.2, and 18.5% higher than that of M0; the compressive strengths of S1-S4 were 23.69, 25.39, 23.59, and 21.73 MPa, respectively, which were 56.8, 68.0, 56.1, and 43.8% higher than that of

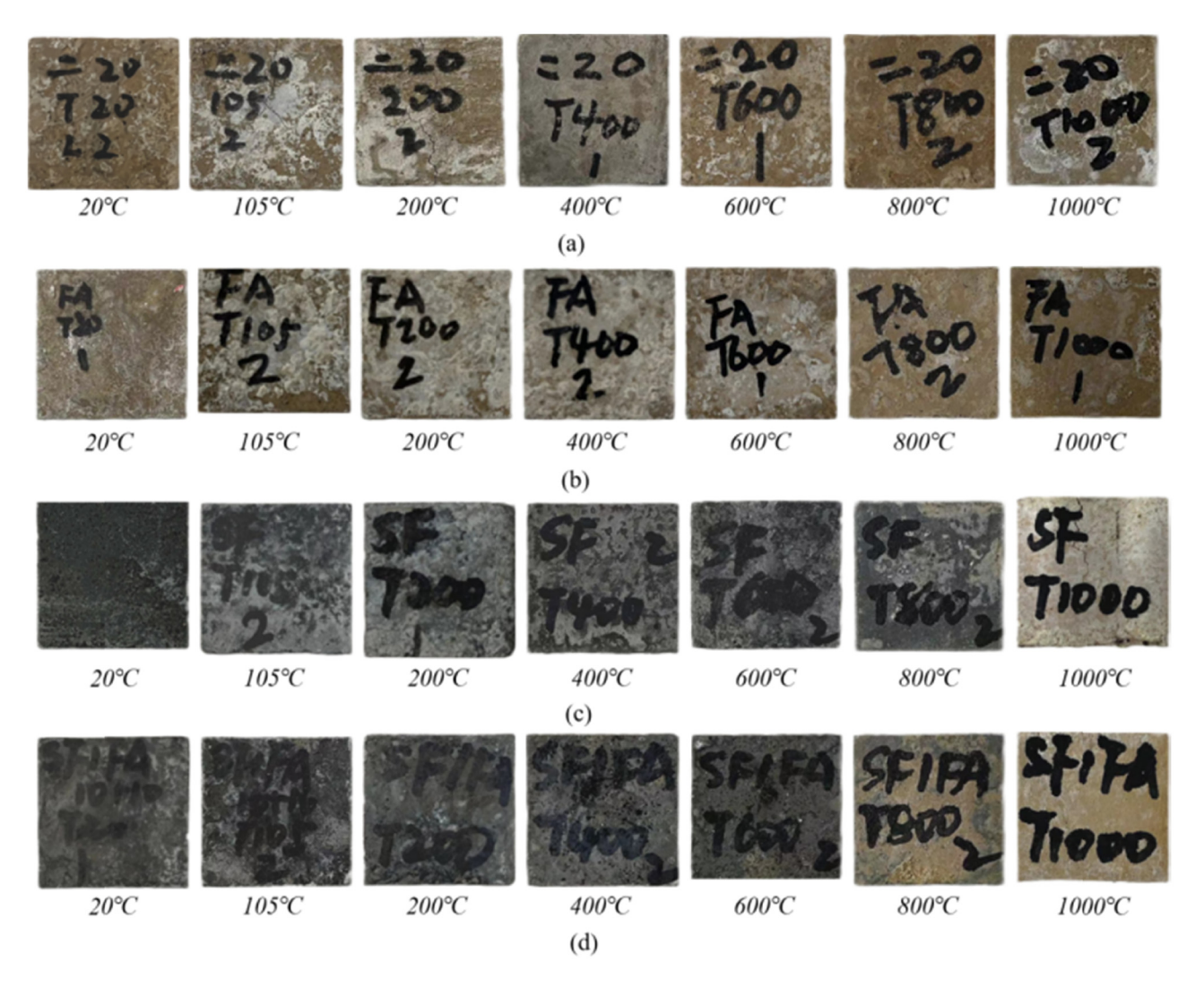


Figure 4: Apparent characteristics of MPC after being treated at different temperatures. (a) M0, (b) F2, (c) S4, and (d) C2.

M0, respectively; and the compressive strengths of C1 and C2 were 29.57 and 30.81 MPa, respectively, which were 95.7 and 103.9% higher than that of M0. This is because when the temperature was 1,000°C, the MPC was sintered and melted, resulting in a denser microstructure of the MPC, which improved the compressive strength [27,35]. This result indicated that FA and SF can improve the compressive strength of MPC after being treated at high temperatures, and the high-temperature resistance of MPC modified by an equal proportion of FA and SF is the best.

Through regression analysis, the relationship between the dimensionless compressive strength and temperature can be obtained, as shown in Figure 6. In the figure, f_c and f_c^T represent the compressive strength of MPC after natural curing at different temperatures, respectively; T refers to

the action temperature; a_0 , a_1 , a_2 , a_3 , and a_4 are the model coefficients, as presented in Table 3.

3.3 Peak strain

Figure 7 shows the peak strain of MPC after being treated at different temperatures. As can be observed, during the implementation of natural curing, the maximum peak strain of S2 was 4.38×10^{-3} , and the minimum peak strain of M0 was 2.39×10^{-3} . The peak strain of MPC with mineral admixtures was higher than that of MPC without admixture. This effect could be ascribed to the fact that the FA and SF particles have a relatively rounded surface and are attached to the pores of the MPC and the FA and SF

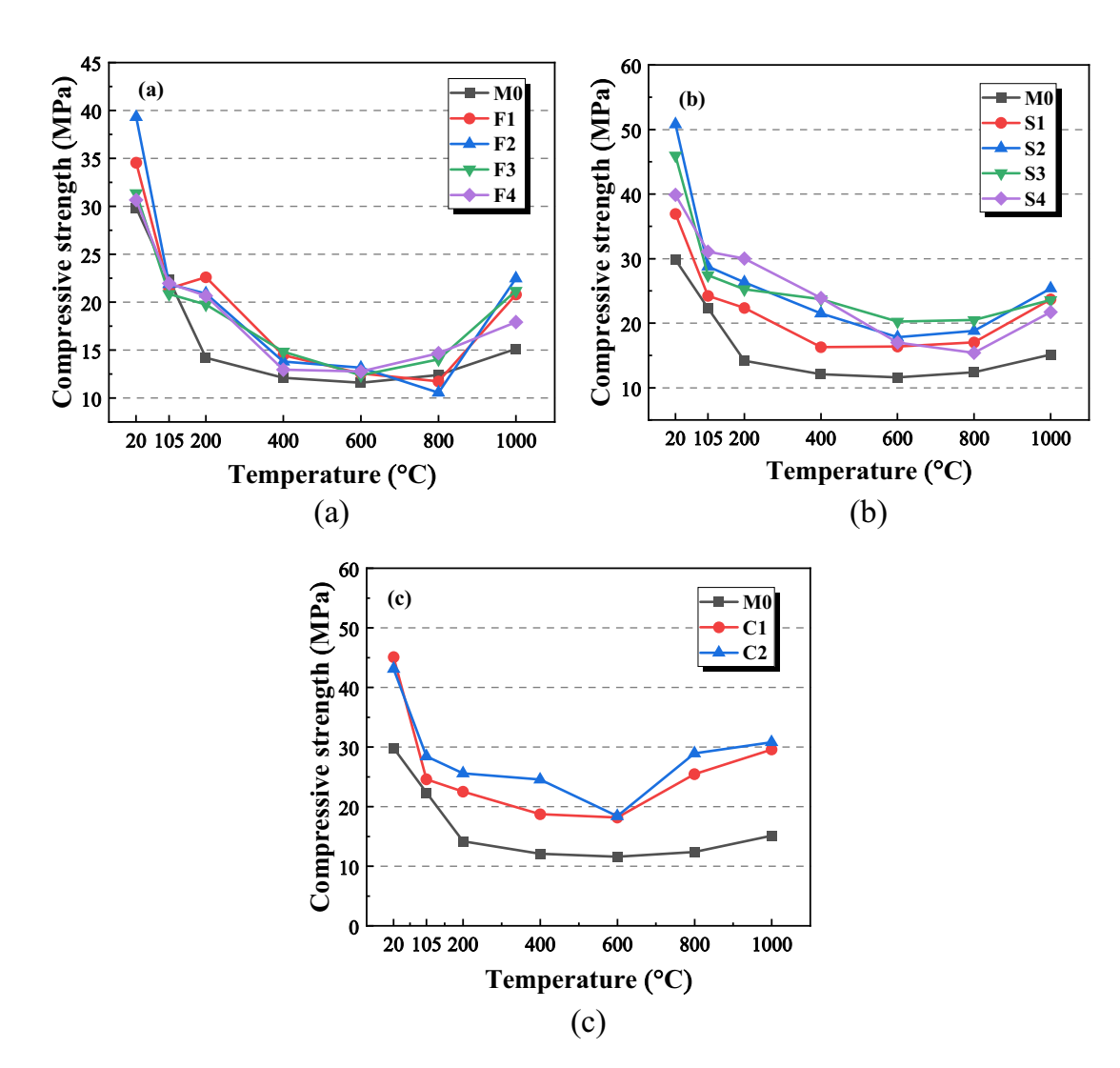


Figure 5: Compressive strength of MPC after being treated at different temperatures. (a) FA-modified MPC, (b) SF-modified MPC, and (c) FA- and SF-modified MPC.

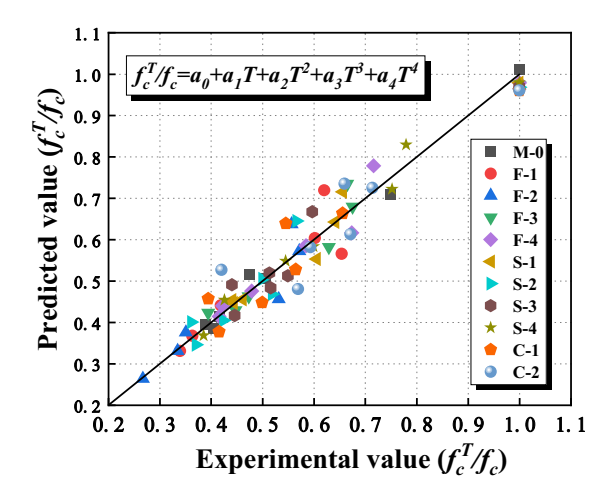


Figure 6: Comparison of the experimental test and model predicted compressive strength results.

particles between the hydration products. As a result, the rapid development of microcracks and increased deformation under loading are induced [32,36].

Although the peak strain of MPC increased with the temperature, this effect was insignificant. When the acting temperature was 20–400°C, the peak strain of M0 gradually increased with increases in the temperature. At 400°C, the peak strain of M0 and MPC mixed with FA reached the maximum value, where M0 was 4.50×10^{-3} , which was 88.3% higher than that of natural curing; the peak strain of MPC with 10-40% FA was 4.57×10^{-3} , 4.08×10^{-3} , 4.02×10^{-3} , and 4.09×10^{-3} , respectively, which was 29.8, 11.2, 40.1, and 43.5% higher than that of natural curing. When the temperature exceeded 600°C, the peak strain of MPC with SF was significantly higher than that of other groups. At 800°C, the peak strain of MPC with 5% SF reached the

Table 3: Related parameters of the compressive strength prediction model

Group	a_0	a_1	a_2	a_3	a_4	R^2
M0	1.10518	-0.0049	1.2094 × 10 ⁻⁵	0^{-5} -1.2904×10^{-8} 5.1073×10^{-12}		0.98851
F1	1.04435	-0.0041	1.1492×10^{-5}	-1.5286×10^{-8}	7.4917×10^{-12}	0.93809
F2	1.08471	-0.0059	1.8452×10^{-5}	-2.4852×10^{-8}	1.1821×10^{-11}	0.96223
F3	1.04786	-0.0039	1.0353×10^{-5}	-1.2860×10^{-8}	6.0738×10^{-12}	0.96369
F4	1.03527	-0.0029	4.4876×10^{-6}	-2.7630×10^{-9}	7.1126×10^{-13}	0.96926
S1	1.06314	-0.0044	1.1841×10^{-5}	-1.4106×10^{-8}	6.2479×10^{-12}	0.97061
S2	1.07335	-0.0056	1.6805×10^{-5}	-2.1290×10^{-8}	9.5239×10^{-12}	0.95181
S3	1.07189	-0.0054	1.7127×10^{-5}	-2.2071×10^{-8}	9.8093×10^{-12}	0.9477
S4	1.02585	-0.0024	6.1344×10^{-6}	-9.0798×10^{-9}	4.8879×10^{-12}	0.98177
C1	1.06479	-0.0054	1.4689×10^{-5}	-1.5935 × 10 ⁻⁸	6.2828×10^{-12}	0.92447
C2	1.03103	-0.0036	8.1304×10^{-6}	-7.4109×10^{-9}	2.5753×10^{-12}	0.84602

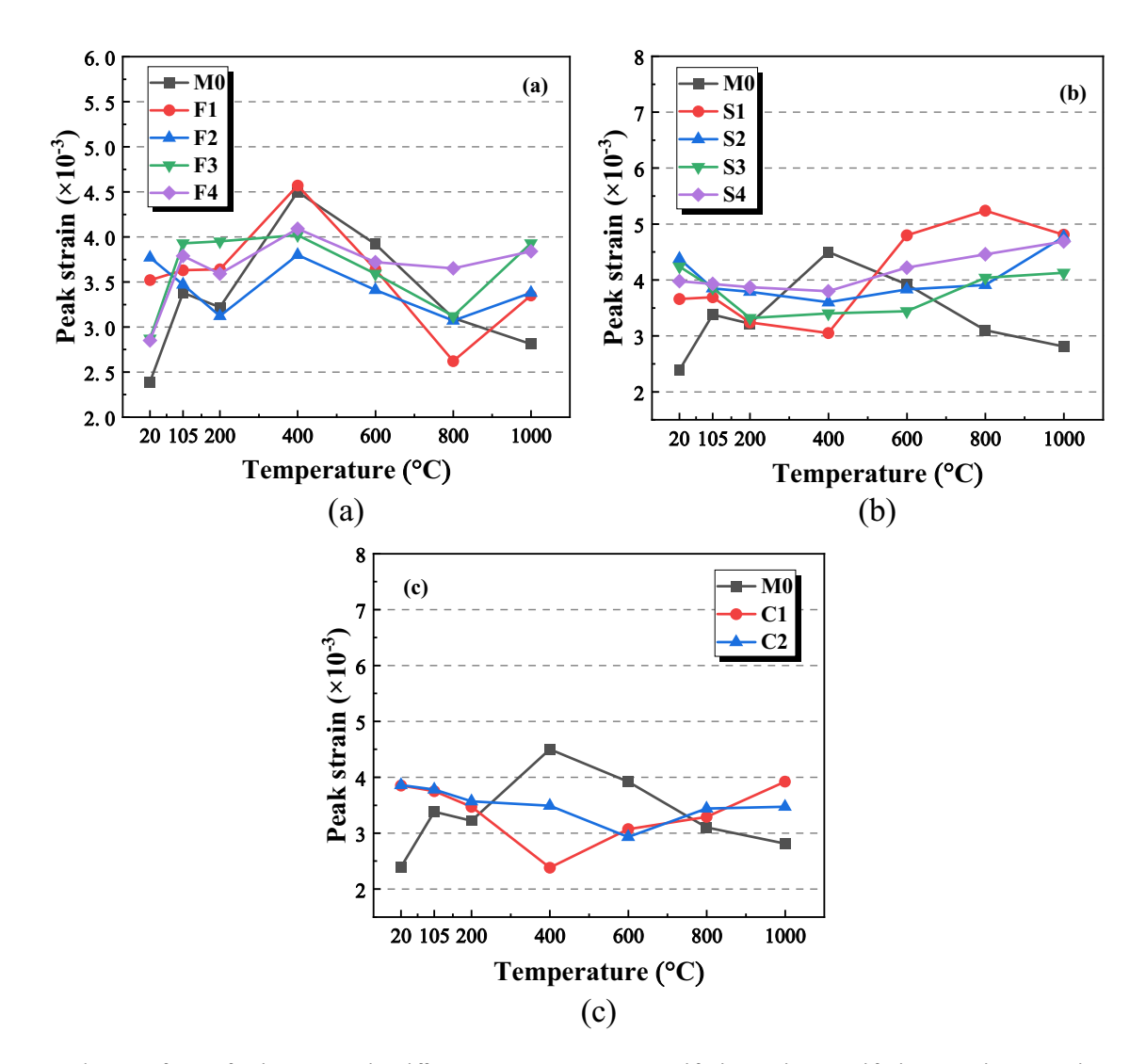


Figure 7: Peak strain of MPC after being treated at different temperatures. (a) FA-modified MPC, (b) SF-modified MPC, and (c) FA- and SF-modified MPC.

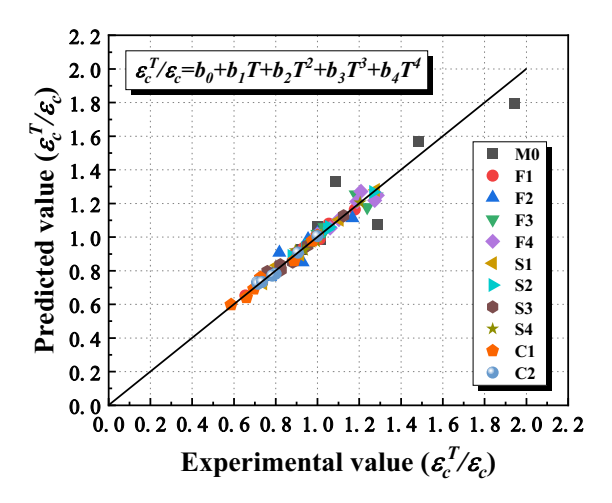


Figure 8: Comparison of peak strain results predicted by the test and model.

maximum value, which was 31.4% higher than that of the natural curing. At 1,000°C, the peak strain of MPC with 10–20% SF reached the maximum value of 9.1, 9.7, and 17.8% higher than that of natural curing. The peak strain of MPC with an equal proportion of FA and SF slightly fluctuated over the entire temperature range and reached a maximum at 1,000°C, which was 102 and 101% of that through natural curing, respectively.

 $\varepsilon_{\rm c}^T/\varepsilon_{\rm c}$ is defined as the dimensionless peak strain. The relationship between the dimensionless peak strain and the temperature can be obtained through nonlinear regression analysis, as depicted in Figure 8. In the formula, $\varepsilon_{\rm c}$ and $\varepsilon_{\rm c}^T$ stand for the peak strains of MPC after natural curing and after action at different temperatures, respectively; T represents the action temperature; and b_0 , b_1 , b_2 , b_3 , and b_4 are the model coefficients, as listed in Table 4.

3.4 Deformation modulus

When calculating the deformation modulus, to reduce the influence of the micro-curve rising section before the elastic stage of the stress–strain curve rises, the deformation modulus between the 0% peak stress and the 90% peak stress in the stress–strain rising section was taken, as shown in Eq. (3).

$$E = \frac{\sigma_{90} - \sigma_0}{\varepsilon_{90} - \varepsilon_0},\tag{3}$$

where E denotes the deformation modulus; σ_{90} and σ_{0} correspond to 90 and 0% of the peak stress, respectively; and ε_{90} and ε_{0} denote the strains corresponding to the 90% peak stress and 0% peak stress, respectively.

The deformation modulus of MPC after action at different temperatures is shown in Figure 9. As can be seen, the deformation modulus of MPC ranged from 10.37 to 12.75 GPa during natural curing, and the highest deformation modulus ratio is M0, indicating that the incorporation of FA and SF reduced the deformation resistance of MPC. With the decrease in the temperature, the deformation modulus exhibited first a trend of decreasing and then increasing, and the deformation modulus of MPC after action at different temperatures was lower than that of natural curing. In the range of 105-400°C, the deformation modulus of M0 decreased by increasing the temperature, and the deformation modulus of M0 at 400°C was the smallest, which was 25.4% of that after natural curing. On the contrary, the deformation modulus of M0 at 600-1,000°C gradually increased by increasing the temperature, and the deformation modulus of M0 at 1,000°C was 5.60 GPa, which was 43.9% of that after natural curing. The deformation modulus of FA-modified MPC after being treated at

Table 4: Related parameters of the peak strain prediction model

Group	b_0	b ₁	b ₂	b ₃	b_4	R^2
M0	2.39166	0.00522	1.0953 × 10 ⁻⁵	-3.9527 × 10 ⁻⁸	2.3778 × 10 ⁻¹¹	0.88803
F1	3.62634	-0.00517	4.7922×10^{-5}	-9.9697×10^{-8}	5.4632×10^{-11}	0.94628
F2	3.85212	-0.00928	4.8370×10^{-5}	-8.0706×10^{-8}	4.1069×10^{-11}	0.81052
F3	2.73487	0.01199	-2.9678×10^{-5}	2.0747×10^{-8}	-1.880×10^{-12}	0.91436
F4	2.75968	0.00938	-2.3321×10^{-6}	2.1046×10^{-9}	-6.028×10^{-11}	0.80576
S1	3.85998	-0.00393	1.3302×10^{-6}	2.9689×10^{-8}	-2.356×10^{-11}	0.91587
S2	4.51475	-0.00825	2.9593×10^{-5}	-3.4407×10^{-8}	1.6746×10^{-11}	0.97614
S3	4.24582	-0.00574	9.5356×10^{-6}	-3.2428×10^{-9}	-3.414×10^{-13}	0.95265
S4	4.01972	-0.00121	5.3542×10^{-7}	5.2731×10^{-9}	-3.986×10^{-12}	0.97669
C1	3.91996	-0.00716	-2.0176×10^{-5}	4.2412×10^{-8}	-2.188×10^{-11}	0.85901
C2	3.73708	0.00168	-1.3841×10^{-5}	2.0498×10^{-8}	-8.234×10^{-12}	0.83724

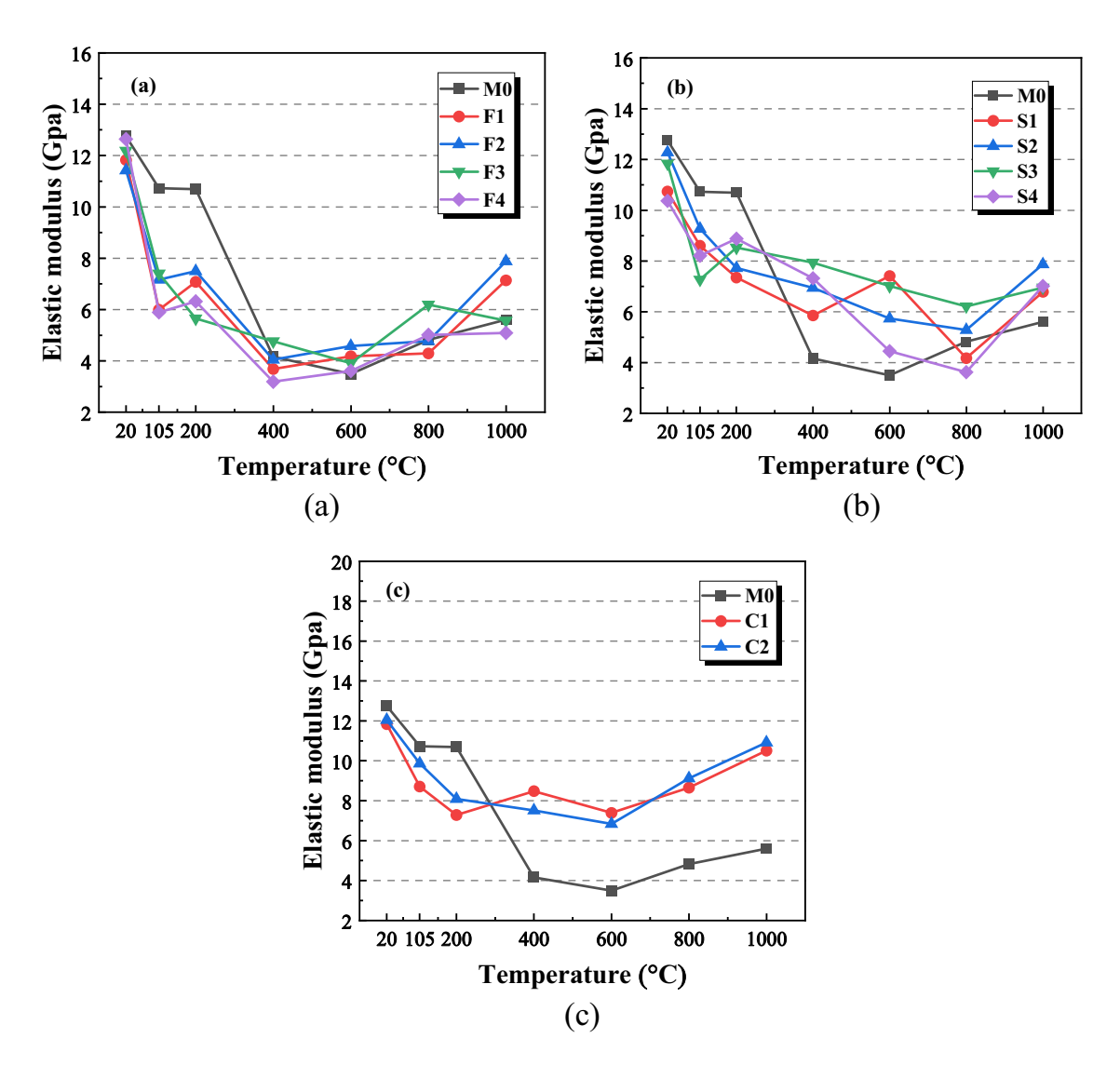


Figure 9: Deformation modulus of MPC after being treated at different temperatures. (a) FA-modified MPC, (b) SF-modified MPC, and (c) FA- and SF-modified MPC.

different temperatures was basically the same as that of M0, which decreased to the lowest at 400°C, and the deformation modulus of F1-F4 were 31, 35.4, 39.0, and 25.4% of that after natural curing, respectively, at 600-1,000°C. Besides, the deformation modulus of FA-modified MPC increased by increasing the temperature, at 1,000°C, and the deformation modulus of F2 reached 7.88 GPa, which was 69.0% of that after natural curing. The deformation modulus of SF-modified MPC decreased to the lowest at 800°C, and the deformation modulus of S1 to S4 were 38.8, 43.0, 52.4, and 34.9% of that after natural curing, respectively. At 1,000°C, and the deformation modulus of S3 reached 6.99 GPa, which was 59.0% of that after natural curing. The deformation modulus of MPC mixed with FA and SF decreased to its lowest value at 600°C, which was 62.4 and 56.8% of that after natural curing, and at 1,000°C, and the

deformation modulus of C1 and C2 were 10.51 and 10.92 GPa, respectively, which were 88.8 and 90.6% of that after natural curing. From the abovementioned analysis, it can be argued that MPC can still maintain a high deformation modulus after experiencing a temperature of 1,000°C because the high temperature causes MPC to form a denser microstructure and improves its deformation resistance [27].

 $E_{\rm c}^T/E_{\rm c}$ is defined as the dimensionless deformation modulus. The relationship between the dimensionless deformation modulus and the temperature can be obtained through nonlinear regression analysis, as shown in Figure 10. In the figure, $E_{\rm c}$ and $E_{\rm c}^T$ represent the MPC deformation modulus under natural curing and MPC deformation modulus under action at different temperatures, respectively; T stands for the operating temperature; and C_0 , C_1 , C_2 , C_3 , and C_4 are the model coefficients, as listed in Table 5.

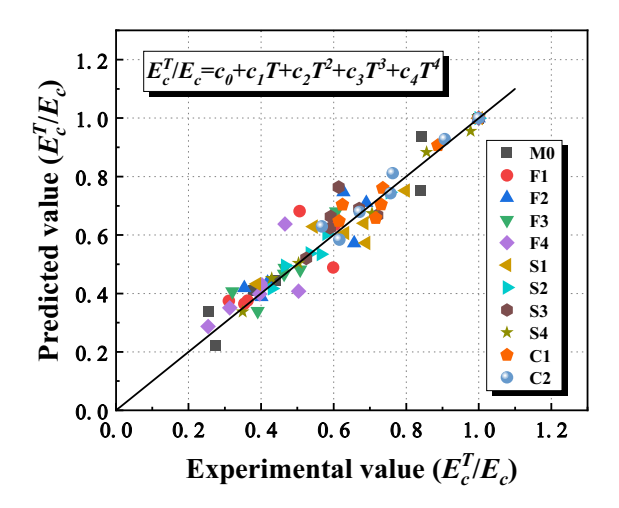


Figure 10: Comparison of the deformation modulus predicted by the test and model.

4 MPC uniaxial compression damage constitutive model

4.1 Stress-strain curve

Figure 11 shows the stress–strain curves of MPC after being treated at different temperatures. As can be seen, the stress–strain curve of MPC rapidly decreased after reaching the peak point during natural curing. After being treated at different temperatures, the slope of the rising section of the stress–strain curve of MPC became smaller, and the rate of decline tended to become gentle. When the temperature increased from 105 to 600°C, the stress–strain curve gradually flattened, and the peak point obviously decreased and shifted to the right. This effect indicated that the peak stress of MPC decreased, the peak strain increased, and the deformation modulus decreased.

When the temperature rose from 600 to 1,000°C, the stress–strain curve of MPC gradually changed from flat to

convex after the high-temperature sintering reaction, the peak stress increased, the peak strain decreased, and the deformation modulus increased.

4.2 Establishing the constitutive model

According to Lemaitre's [37] strain equivalence principle, the strain caused by the effective stress σ^* on the non-destructive material can be expressed as the strain caused by the nominal stress σ on the damaged material. Based on this, the axial compression damage constitutive relation of MPC after high-temperature action can be expressed by using Eqs. (4) and (5) [38–40].

$$E_c^T = E_c (1 - D_c^T)^i, (4)$$

$$\sigma_c^T = E_c (1 - D_c^T)^i \varepsilon^j, \tag{5}$$

where $\sigma_{\rm c}^T$ is the stress of MPC after high temperature, ε denotes the strain, and $D_{\rm c}^T$ refers to the damage variable of MPC after different temperatures. The parameters i and j are model parameters.

After the application of different temperatures, the damage of MPC specimens under axial compression load can be divided into two parts: chemical damage caused by temperature and physical damage caused by axial compression load. According to the principle of strain equivalence, the damage constitutive relation of MPC under axial compression load after different temperatures can be expressed as follows [41,42]:

$$\sigma = E_c^T (1 - D_c)^i \varepsilon^j, \tag{6}$$

where D_c is the damage variable caused by the load.

Substituting Eq. (4) in Eq. (6), the constitutive relationship of MPC axial compression damage after action at different temperatures can be expressed as follows [39]:

$$\sigma = E_{c}[1 - (D_{c} + D_{c}^{T} - D_{c}D_{c}^{T})]^{i} \varepsilon^{j}, \tag{7}$$

Table 5: Related parameters of the deformation modulus prediction model

Group	c_0	c_1	c_2	c_3	c_4	R^2
M0	12.4256	0.00758	-1.6784 × 10 ⁻⁴	3.0493 × 10 ⁻⁷	-1.515 × 10 ⁻¹¹	0.95471
F1	12.4162	-0.06036	1.6592×10^{-4}	-2.0214×10^{-7}	9.1323×10^{-11}	0.87448
F2	11.93083	-0.04446	1.0374×10^{-4}	-1.1685×10^{-7}	5.3512×10^{-11}	0.92076
F3	13.00125	-0.05992	1.3522×10^{-4}	-1.1816 × 10 ⁻⁷	3.5640×10^{-11}	0.9504
F4	13.36831	-0.07089	1.7509×10^{-4}	-1.7461×10^{-7}	6.2188×10^{-11}	0.8994
S1	11.93835	-0.05126	1.8077×10^{-4}	-2.0645×10^{-7}	1.2566×10^{-10}	0.88397
S2	13.29973	-0.05443	1.6411×10^{-4}	-2.1484×10^{-7}	9.8450×10^{-11}	0.98894
S3	12.27512	-0.05141	1.8730×10^{-4}	-2.6699×10^{-7}	1.2587×10^{-10}	0.83145
S4	10.48497	-0.00367	-1.4357×10^{-5}	-8.515×10^{-10}	1.3635×10^{-11}	0.99334
C1	12.63462	-0.05106	1.6840×10^{-4}	-2.1912×10^{-7}	9.9722×10^{-11}	0.89946
C2	12.49862	-0.03451	7.2538×10^{-5}	-6.1764×10^{-8}	2.2223×10^{-11}	0.95465

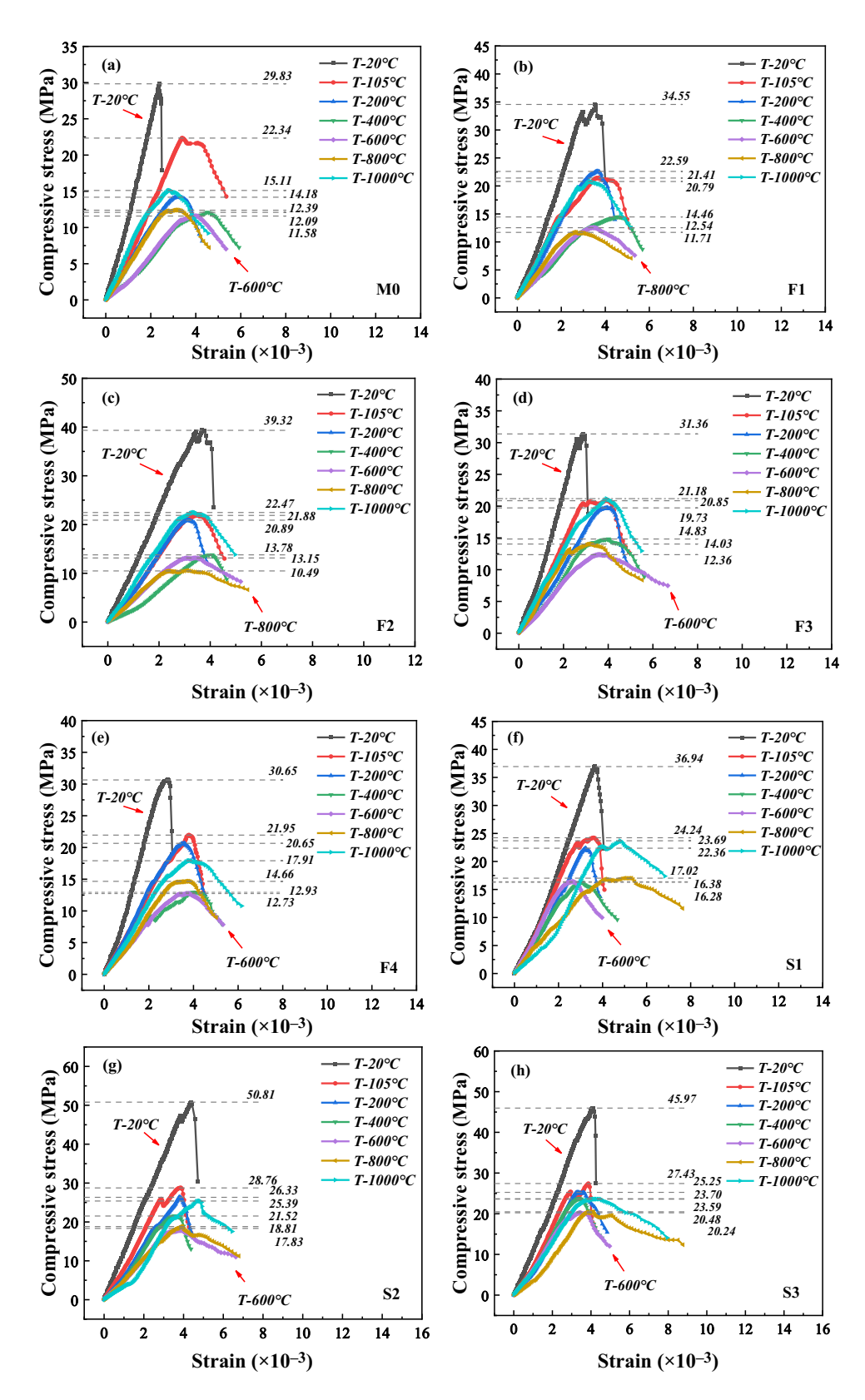


Figure 11: Stress-strain curves of FA/SF modified MPC after being treated at different temperatures. (a) M0, (b) F1, (c) F2, (d) F3, (e) F4, (f) S1, (g) S2, (h) S3, (i) S4, (j) C1, and (k) C2.

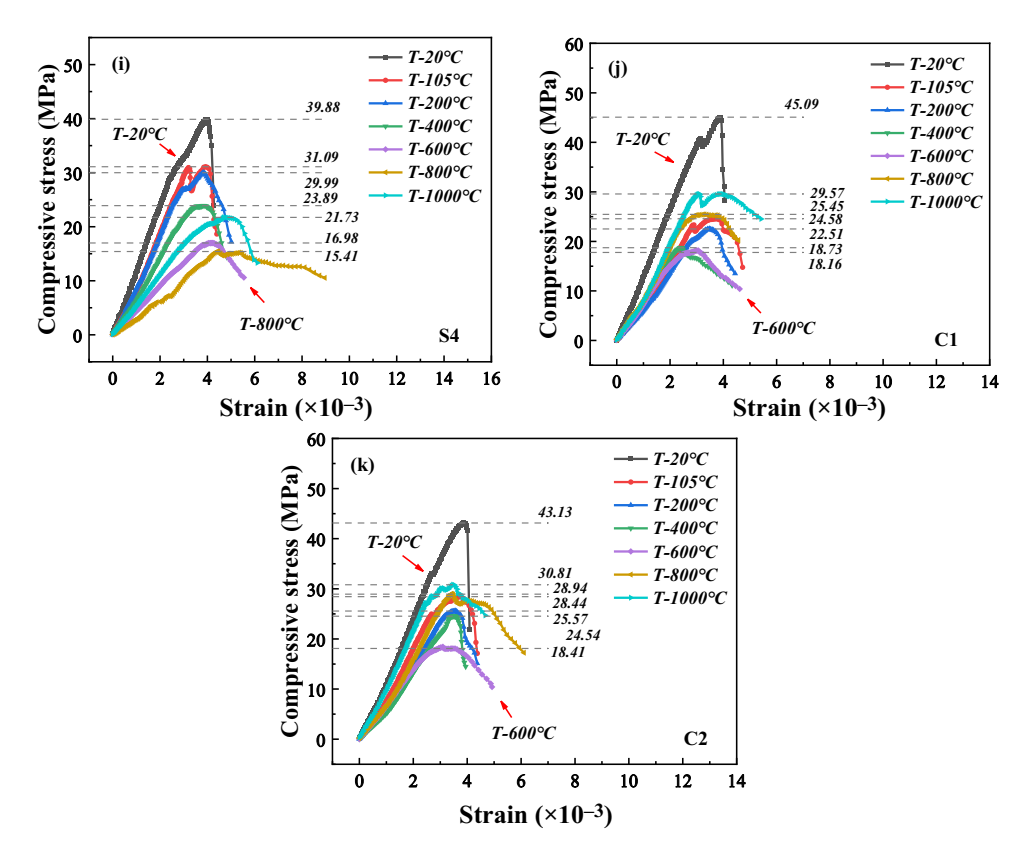


Figure 11: (Continued)

where D is defined as the total damage variable of MPC after action at different temperatures, which can be expressed as follows:

$$D = D_{c} + D_{c}^{T} - D_{c}D_{c}^{T}.$$
 (8)

Then, Eq. (7) can be simplified to the following expression:

$$\sigma = E_c (1 - D)^i \varepsilon^j. \tag{9}$$

According to the macroscopic phenomenological damage mechanics, the degree of damage deterioration inside the MPC can be characterized by its macroscopic physical and mechanical properties. According to Eq. (4), the damage variable of MPC after action at different temperatures can be expressed as follows [38,39]:

$$D_{\rm c}^T = 1 - \frac{E_{\rm c}^T}{E_{\rm c}}. (10)$$

During the process of pouring and hardening, various defects are inevitably induced within MPC, such as micropores and microcracks. When subjected to loading, the damage caused by the various defects is also randomly distributed within the active core of the MPC materials [42]. Considering that the damage to MPC during the

loading process is continuous, MPC can be regarded as a whole composed of numerous small meso-elements, and its damage degree is related to the cumulative damage number of each meso-element. It can be assumed that the strength $\varphi(\varepsilon)$ of each meso-element of MPC obeys the Weibull distribution, and its probability density function can be expressed as follows [38,40,41]:

$$\varphi(\varepsilon) = \frac{\alpha}{\lambda} \left(\frac{\varepsilon}{\lambda} \right)^{\alpha - 1} \exp \left[-\left(\frac{\varepsilon}{\lambda} \right)^{\alpha} \right], \tag{11}$$

where α and λ are the Weibull distribution parameters.

During the process of the MPC axial compression test, it can be assumed that the number of micro-elements destroyed by MPC under a certain level of pressure load is n. In addition, the damage variable $D_{\rm c}$ caused by loading can be defined as the ratio of the number of micro-elements destroyed to the total number of micro-elements. Therefore, the damage variable $D_{\rm c}$ caused by loading can be expressed as follows [39]:

$$D_{\rm c} = \frac{n}{N},\tag{12}$$

where N is the total number of micro-elements of the MPC specimen.

Under a certain axial compression load, the number of micro-elements damaged n and the total number of micro-elements N in MPC can be expressed as follows:

$$n = N \int_{0}^{\varepsilon} \varphi(x) = N \left\{ 1 - \exp\left[-\left(\frac{\varepsilon}{\lambda}\right)^{\alpha} \right] \right\}. \tag{13}$$

The damage variable D_c of MPC under loading can be expressed using Eqs. (12) and (13).

$$D_{\rm c} = 1 - \exp\left[-\left(\frac{\varepsilon}{\lambda}\right)^{\alpha}\right]. \tag{14}$$

By substituting Eqs. (10) and (14) in Eq. (8), the total damage variable *D* of MPC under loading at different temperatures can be obtained, which is expressed by Eq. (15).

$$D = 1 - \frac{E_{\rm c}^T}{E_{\rm c}} \exp\left[-\left(\frac{\varepsilon}{\lambda}\right)^{\alpha}\right]. \tag{15}$$

By substituting Eq. (15) in Eq. (9), the MPC axial compressive damage constitutive model modified by FA/SFs at different temperatures can be obtained.

$$\sigma = \frac{\left[E_c^T \exp\left[-\left(\frac{\varepsilon}{\lambda}\right)^{\alpha}\right]\right]^{i} \varepsilon^{j}}{E_c^{i-1}}.$$
 (16)

4.3 Physical interpretation and variation in the constitutive model parameters

When other conditions remain unchanged, the impact of parameters α , λ , i, and j on the axial compression stressstrain curve of MPC is illustrated in Figure 12(a)–(d). The parameters α and λ are Weibull distribution parameters, and from Figure 12(a) and (b), it can be observed that with an increase in parameters α and λ , the shape of the stressstrain curve exhibits no obvious changes; the peak strain and peak stress decrease with increasing parameter α , increase with a further increase in the parameter λ . The parameter i is a parameter describing the brittle characteristics of the MPC stress–strain curve. As can be seen

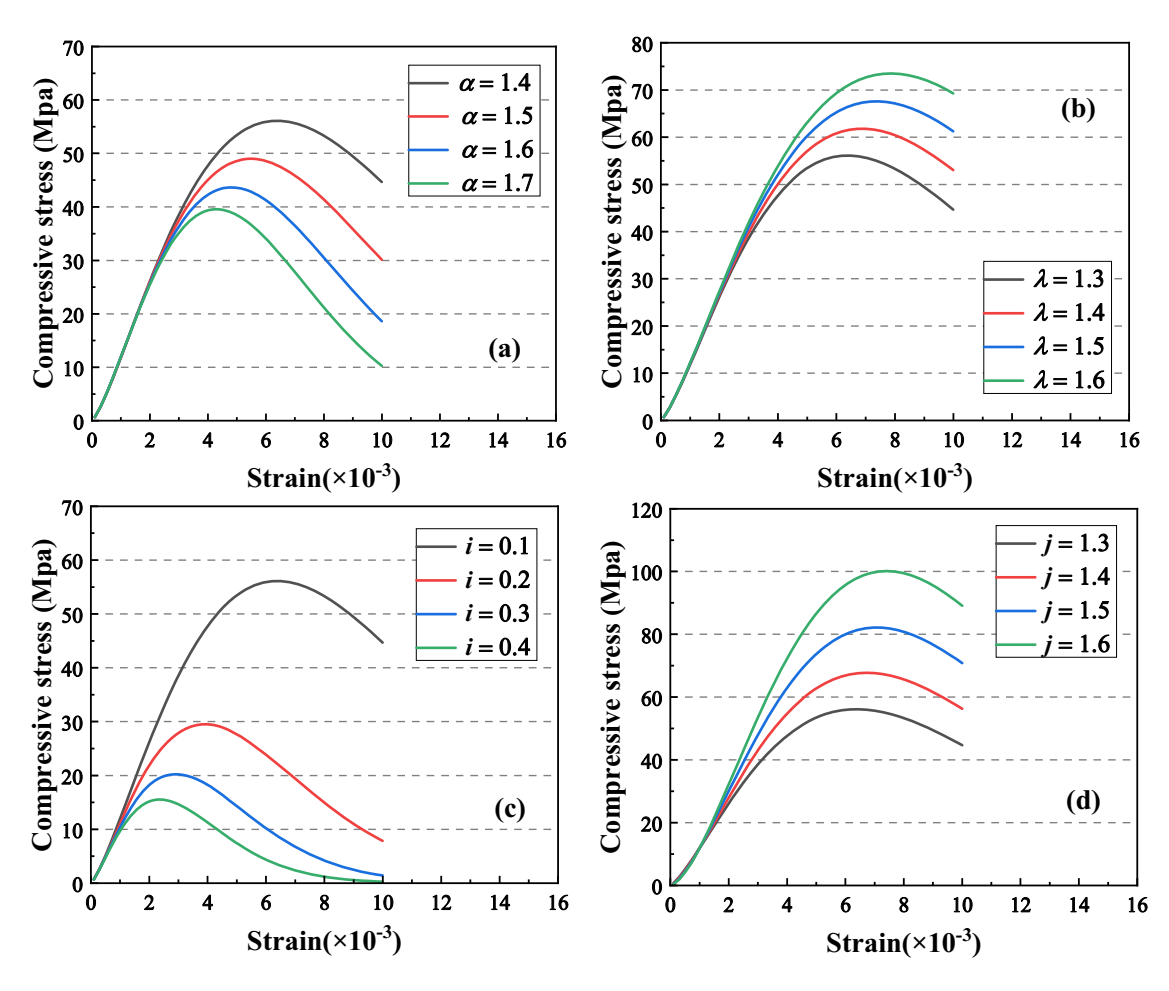


Figure 12: Physical interpretation and variation law of MPC axial compression constitutive model parameters. (a) parameter α , (b) parameter λ , (c) parameter i, (d) parameter i.

14 — Boyu Guo et al.

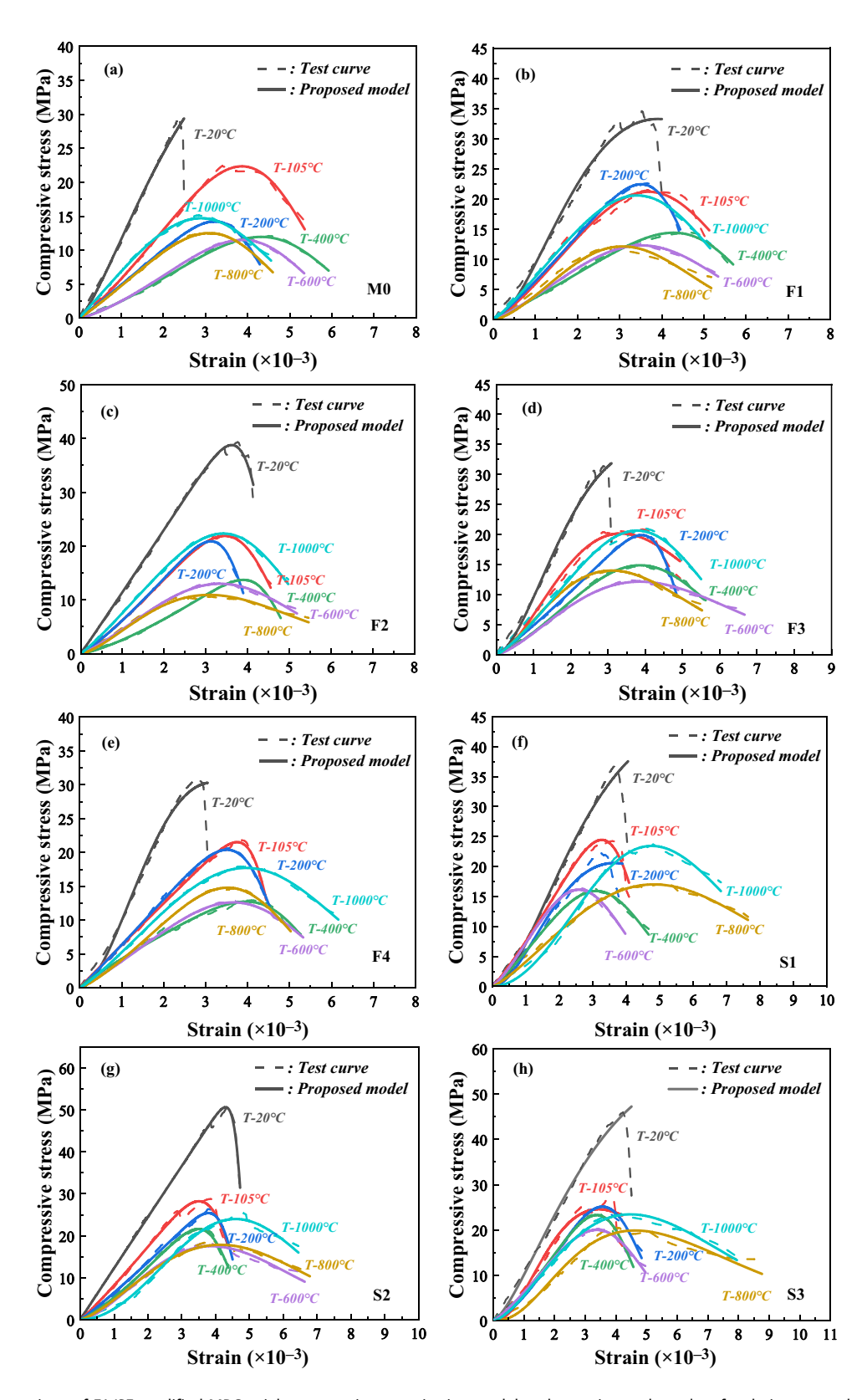


Figure 13: Comparison of FA/SF modified MPC axial compression constitutive model and experimental results after being treated at different temperatures. (a) M0, (b) F1, (c) F2, (d) F3, (e) F4, (f) S1, (g) S2, (h) S3, (i) S4, (j) C1, and (k) C2.

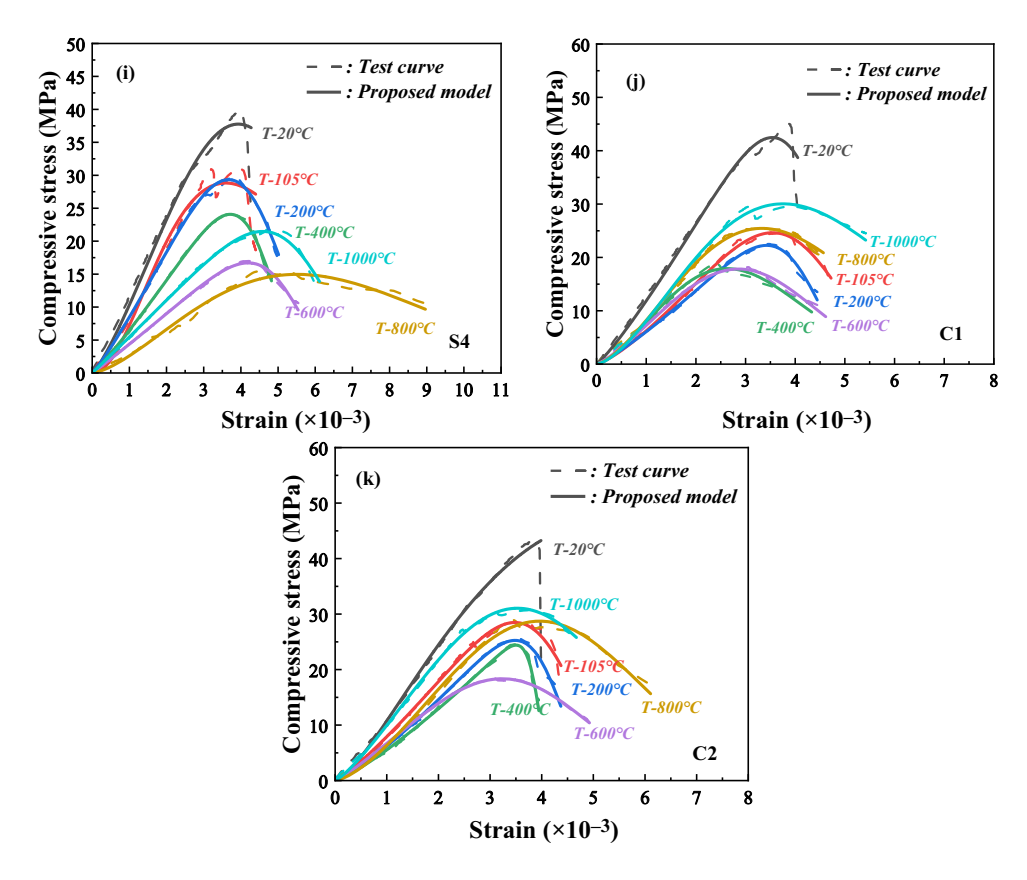


Figure 13: (Continued)

from Figure 12(c), as the value of parameter i increases, the proportion of the elastic rising stage of the stress–strain curve increases. However, the slope of the falling section of the curve increases and the rate of decline becomes bigger. Parameter j reflects the peak stress of MPC. It can be seen from Figure 12(d) that, with an increase in parameter j, the stress–strain curve is not significantly changed, and the peak stress significantly increases.

4.4 Comparison of constitutive model and experimental results

The axial compression constitutive model Eq. (16) for MPC established in this work after the action at different temperatures was compared with the stress–strain relationship obtained from the tests, as shown in Figure 13. As can be seen from Figure 13, the predicted curve of the MPC axial compression constitutive model after being treated at different temperatures is basically consistent with the test curve, and the predicted curve is more consistent with the test curve in the rising stage. Table 6

presents the relevant parameters of the prediction model. It can be observed that the correlation coefficient of the prediction model increased when the temperature increased. Moreover, the correlation coefficient of the prediction model was more than 0.98 for the best prediction effect when it was greater than 600°C, and when it was less than 600°C, the correlation coefficient of the prediction model was greater than 0.97. Therefore, the established axial compression constitutive model can better predict the axial compression stress—strain relationship of FA- and SF-modified MPC after 20–1,000°C temperature action.

4.5 Evolution characteristics of the damage variables

According to the Eq. (15), the total damage variable D value of MPC under axial compression after action at different temperatures can be calculated. Figure 14 depicts the relationship between the total damage variable D of MPC and strain ε . As can be observed from Figure 14, the D value $(D_{\varepsilon,\text{Max}})$ corresponding to the peak strain of M0 at 20°C was

 Table 6: Related parameters of the MPC axial compression constitutive model after being treated at different temperatures

Group	Data in formula	20°C	105°C	200°C	400°C	600°C	800°C	1,000°C
M0	α	2.70792	4.7324	6.58195	4.83253	4.64435	3.93891	3.16157
	λ	6.86501	6.79094	5.34176	4.87834	3.79528	1.56654	5.55609
	i	0.13536	3.60895	4.43173	0.46644	0.25981	0.01924	2.51056
	j	1.29866	1.18796	1.0475	1.25497	1.33974	1.10882	1.01706
	R^2	0.98305	0.99759	0.99941	0.99761	0.99882	0.99914	0.99803
F1	α	1.4801	3.47774	7.00308	5.6331	3.17869	2.5506	3.43412
	λ	4.16815	2.93743	3.60925	1.79548	1.8656	1.626	1.6688
	i	0.26383	0.00169	0.19613	0.00143	0.0502	0.00328	0.00202
	j	1.77684	1.24452	1.12767	1.07105	1.20034	1.46858	1.13119
	R^2	0.98243	0.96989	0.99893	0.99674	0.99867	0.96605	0.99836
F2	α	11.3129	6.48902	9.40026	10.6382	3.15216	1.80652	3.97745
	λ	4.8615	3.76413	3.58268	4.39528	1.50786	0.79094	2.73618
	i	0.00455	0.31315	0.45561	0.44475	0.0027	0.00341	0.11483
	j	1.01406	1.16354	1.17713	1.32565	1.20198	1.45333	1.10775
	R^2	0.99781	0.9994	0.99926	0.99893	0.99735	0.98081	0.99908
F3	α	1.24715	1.74166	10.6178	3.38509	2.0105	1.92336	3.4592
	λ	4.81229	1.70548	4.14265	3.43445	0.91938	0.64161	1.62984
	i	1.74227	0.00502	0.19773	0.25925	0.02955	0.00317	0.00201
	j	1.73942	1.58104	1.11306	1.30838	1.39841	1.33646	1.26043
	R^2	0.97697	0.9845	0.99845	0.99737	0.99723	0.99651	0.98352
F4	α	1.82615	13.7876	7.45736	6.5839	3.87273	4.19055	3.028
	λ	4.25066	4.18113	3.90185	3.87815	0.99408	4.17066	2.28224
	i	0.00218	0.31925	0.30915	0.11732	0.00187	0.60023	0.07209
	j	1.8343	0.98181	1.04189	0.89225	1.12863	1.24932	1.15908
	R ²	0.98097	0.99715	0.99858	0.9901	0.99885	0.99883	0.99891
S1	α	1.28036	6.90047	2.71676	3.57079	3.3183	2.24316	2.26237
	λ	4.69745	3.97005	4.11784	1.24181	1.43468	1.33757	4.03899
	i	0.42586	0.62664	0.01526	0.00213	0.02752	0.00234	2.11226
	j	2.03071	1.13767	1.92017	1.17595	1.22959	1.24736	1.97611
	R ²	0.97754	0.99449	0.96145	0.99814	0.99745	0.99138	0.99304
S2	α	2.80314	8.50385	13.5533	8.35397	2.00723	2.24005	2.63585
	λ	4.49492	4.06545	4.25418	4.01126	2.24595	1.78969	4.26578
	i	0.00168	0.44833	0.38948	0.47595	0.25565	0.09061	2.45477
	i	0.9945	1.08939	1.09099	1.24439	1.53286	1.32853	1.92798
	R ²	0.99868	0.99043	0.99585	0.99805	0.98808	0.99318	0.99322
S3	α	1.37629	2.35399	4.97792	5.77777	3.95685	1.49839	1.58015
33	λ	5.03128	3.33991	4.92436	4.1128	3.16017	2.63942	2.22671
	i	0.17145	0.19967	1.45502	0.70001	0.23456	0.19144	0.26108
	j	1.47531	2.47318	1.45438	1.29752	1.21327	2.81041	1.5636
	R ²	0.98418	0.96817	0.99694	0.99721	0.99793	0.98259	0.99285
S4	α	2.06122	2.40797	4.94293	6.98622	6.6905	1.81749	5.59891
34	λ	5.18037	1.56252	3.8986	4.16085	3.17348	3.0843	4.74406
	i	0.01017	0.00617	0.30897	0.35442	0.02415	0.28412	0.64112
	j	1.23931	2.15417	1.13219	1.12333	1.04533	1.4844	1.01906
	r ²	0.98492	0.97218	0.99771	0.99908	0.9984	0.98699	0.99761
C1	α	6.45876	4.75953	7.26538	2.41655	2.90407	2.13736	1.91561
Ci	λ	5.48129	4.73775	3.84532	1.27158	0.87942	0.80944	2.44653
	i	0.01323	1.08552	0.38072	0.00436	0.00259	0.00203	1.65447
	i	1.15128	1.30006	1.19095	1.45335	1.24659	1.46703	1.55586
	J R ²	0.98613	0.99621	0.99779	0.98968	0.99696	0.99336	0.99337
C2	α	1.60291	6.1153	8.95697	23.6178	3.33051	2.81507	2.87333
C2	λ	5.68325	4.63914	4.15913	3.89969	1.63193	5.43452	4.45684
		0.04499		0.6733	0.65057	0.02851	1.26957	0.83866
	i i		1.12101					
	j n ²	1.43242	1.18399	1.23703	1.22634	1.14621	1.46884	1.23396
	R^2	0.98187	0.99518	0.99646	0.99755	0.99939	0.99308	0.99765

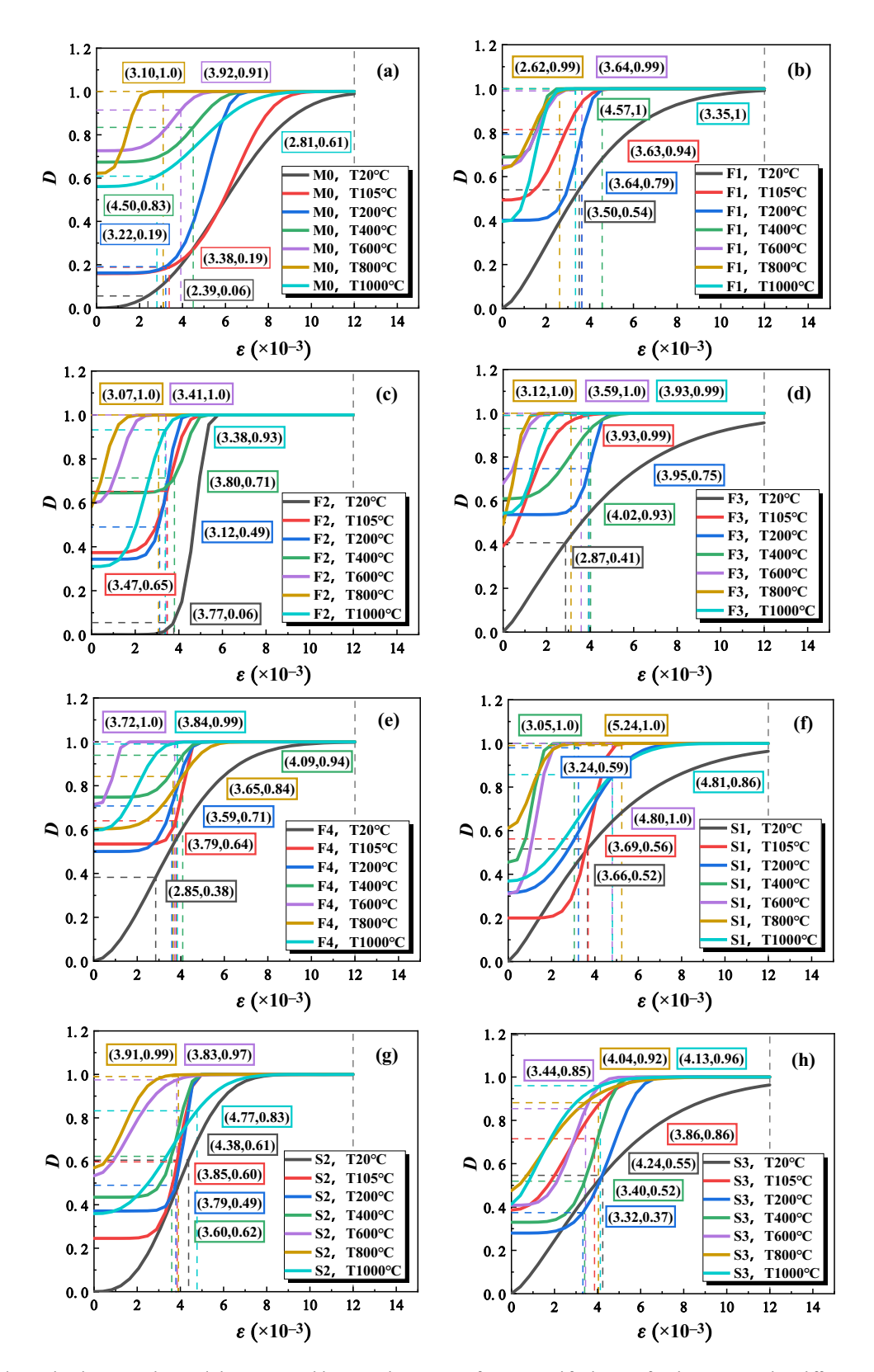


Figure 14: Relationship between the total damage variable (D) and strain (ε) of FA/SF modified MPC after being treated at different temperatures. (a) M0, (b) F1, (c) F2, (d) F3, (e) F4, (f) S1, (g) S2, (h) S3, (i) S4, (j) C1, and (k) C2.

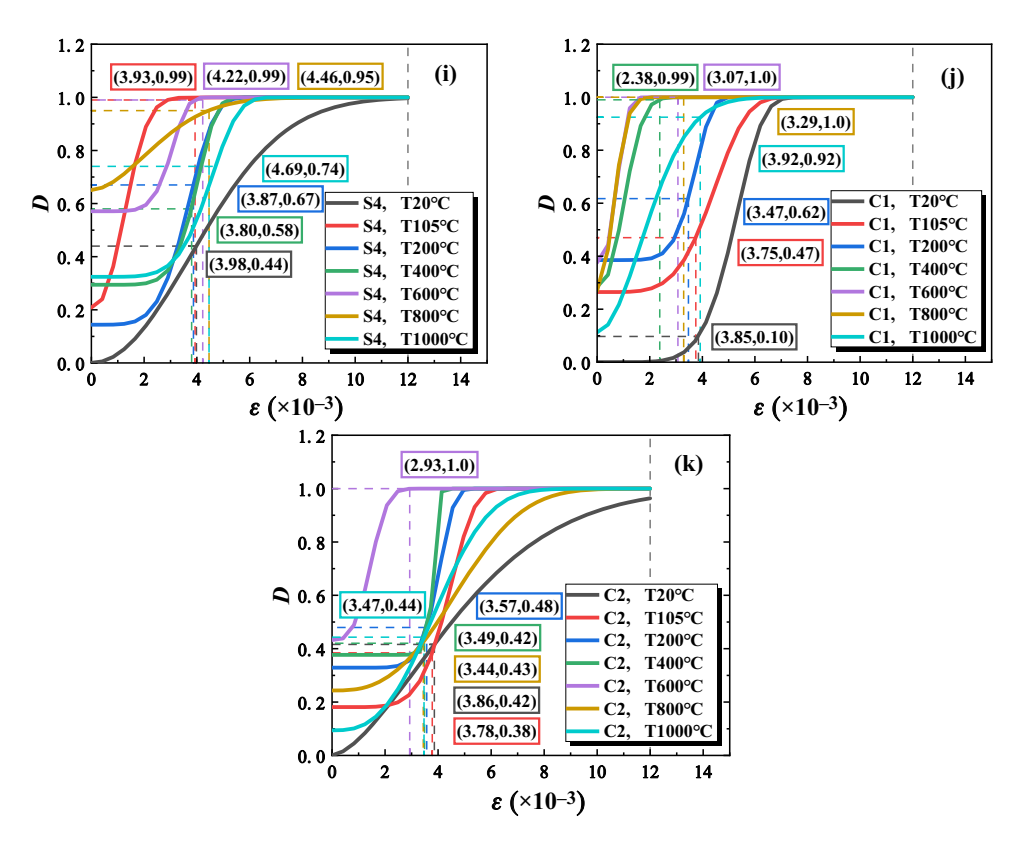


Figure 14: (Continued)

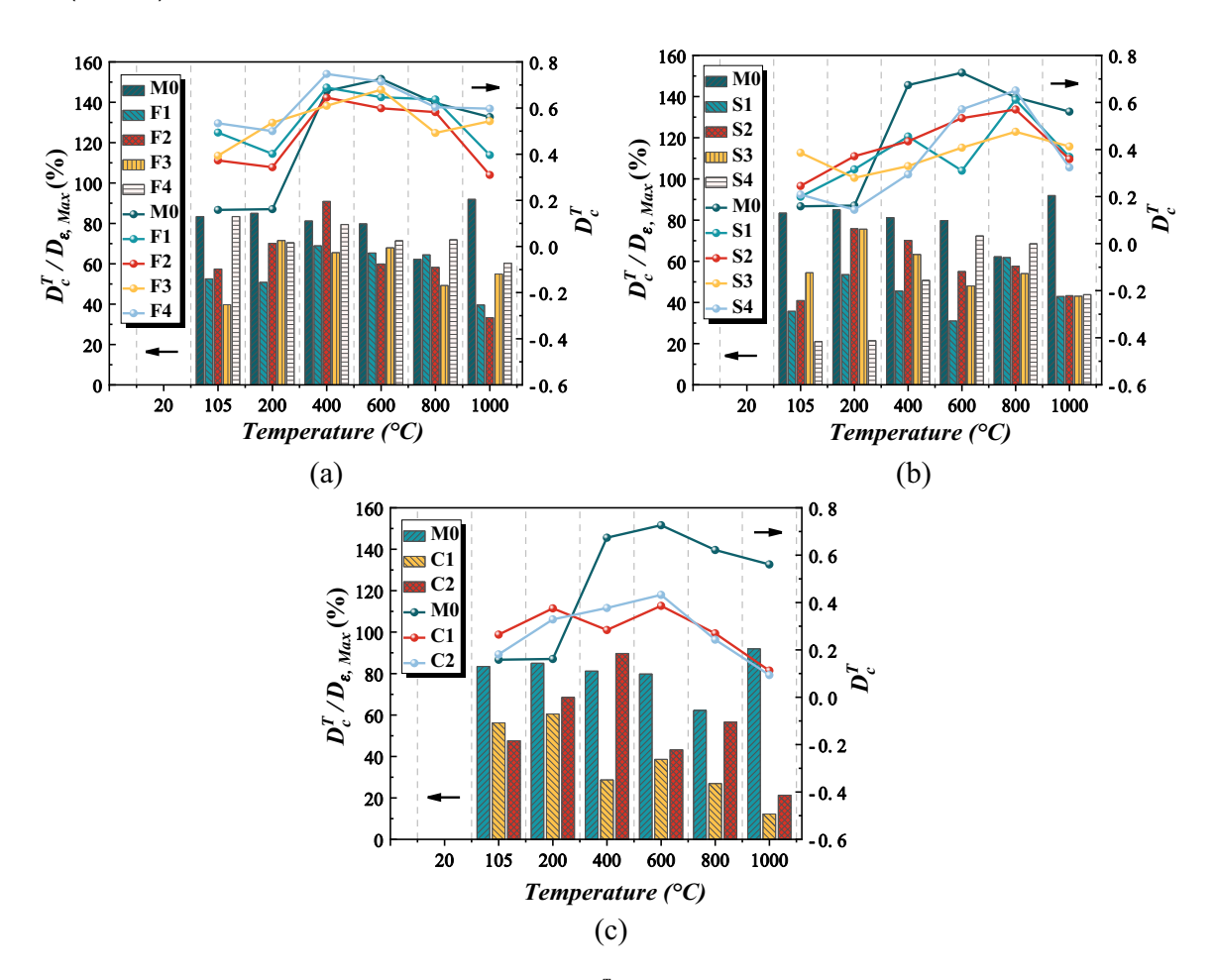


Figure 15: The relationship between the temperature damage variable D_c^T and $D_{\varepsilon, \text{Max}}$ of MPC. (a) FA-modified MPC, (b) SF-modified MPC, and (c) FA-and SF-modified MPC.

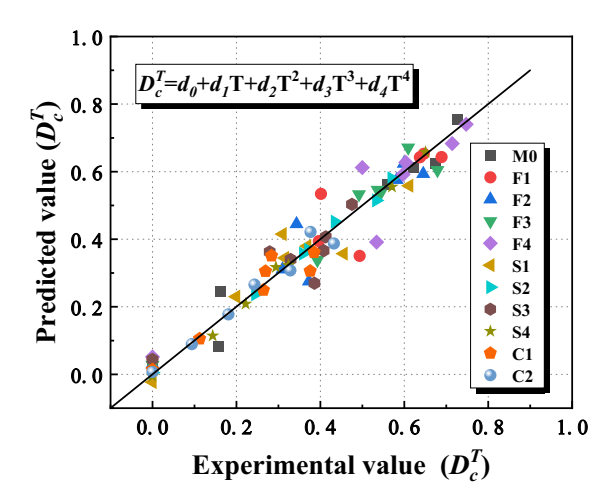


Figure 16: Comparison of $D_{\rm c}^T$ values predicted by the experiment and the model.

0.06; as the temperature increased, the $D_{\varepsilon, \text{Max}}$ increased and then decreased, and the inflexion point occurred at 800°C as 1.0. This result indicates that the damage to the specimen is serious, and the value of $D_{\varepsilon, \text{Max}}$ for M0 was 0.61 at 1,000°C. The $D_{\varepsilon,\text{Max}}$ values of F1–F4 were higher than M0 at 20°C, 0.54, 0.06, 0.41, and 0.38, respectively, and the trend of $D_{\varepsilon,\mathrm{Max}}$ values with temperature was approximately the same as that of M0. The $D_{\varepsilon,\mathrm{Max}}$ values of F1 reached a maximum value of 0.99 at 400°C, and those of F2-F4 all reached a maximum value of 1.0 at 600°C; at 1,000°C the $D_{\varepsilon,\mathrm{Max}}$ values of F1–F4 were 1.0, 0.93, 0.99, and 0.99, respectively. At room temperature, the $D_{\varepsilon,\text{Max}}$ values of S1–S4 were higher than those of other groups, at 0.52, 0.61, 0.55, and 0.44, respectively, which were 0.46, 0.55, 0.49, and 0.38 higher than those of M0. The $D_{\varepsilon,\text{Max}}$ values of S1–S4 reached a maximum at 600°C, at 1.0, 0.97, 0.85, and 0.99, respectively, and 0.86, 0.83, 0.96, and 0.74 at 1,000°C. The maximum $D_{\varepsilon, \text{Max}}$ values of C1 and C2 also appeared at 600°C, which were 1.0, and 0.92 and 0.44 at 1,000°C, respectively.

When not loaded, the initial temperature damage exists in the MPC after different temperatures, suggesting that the damage caused by the temperature action of the MPC is cumulative and irreversible. Besides, the damage variable D remains basically unchanged at the beginning of the loading period. By increasing the load, the damage variable D rises with the increase in the load after a certain damage threshold is reached in front of the peak strain, and the overall strain ε shows an "S-type" trend of change. By further increasing the temperature, the rise speed of the D value first increases and then decreases.

To further analyse the influence of the temperature on the damage evolution characteristics of MPC, the temperature damage variable D_c^T of MPC after the action at different temperatures was calculated using Eq. (10), as dispelled in Figure 15. It can be seen that the temperature damage variable D_c^T of MPC presented a changing trend of first increasing and then decreasing with an increase in the acting temperature, and the rising stage was mainly concentrated in the range of 20-600°C. This could be due to the decomposition of MgKPO₄·6H₂O, the hydration product of MPC, along with free water evaporation, which lead to an increase in the number of pores and internal defects in the specimen [29,35]. When the temperature was higher than 600°C, the D_c^T value gradually decreased owing to the sintering effect of the temperature leading to the transformation of the hydrated product crystal of MPC; this yields a denser microstructure inside the MPC.

When the temperature was lower than 200°C, the $D_{\rm c}^T$ value of M0 was the lowest at 105 and 200°C, with the extracted $D_{\rm c}^T$ values being 0.158 and 0.162, which were 83.4 and 85% of $D_{\rm c,Max}$. This effect points out that the damage to M0 in this temperature range was mainly caused by the action of the temperature. As the temperature increased to 600°C, the temperature damage variable $D_{\rm c}^T$ of each group of specimens reached more than 30% of the

Table 7: D_c^T value prediction model-related parameters

Group	d_0	d_1	d_2	d_3	d_4	R^2
M0	0.02705	-4.727 × 10 ⁻⁴	1.154 × 10 ⁻⁵	-2.059 × 10 ⁻⁸	1.006 × 10 ⁻¹¹	0.96852
F1	-0.04965	0.00512	-1.403×10^{-5}	1.709×10^{-8}	-7.719×10^{-12}	0.87448
F2	-0.04471	0.00389	-9.104×10^{-6}	1.027×10^{-8}	-4.708×10^{-12}	0.92096
F3	-0.06625	0.00491	-1.102×10^{-5}	9.537×10^{-9}	-2.822×10^{-12}	0.95015
F4	-0.05267	0.00546	-1.302×10^{-5}	1.253×10^{-8}	-4.332×10^{-12}	0.90018
S1	-0.11174	0.00476	-1.677×10^{-5}	2.416×10^{-8}	-1.166×10^{-11}	0.88371
S2	-0.07101	0.00404	-1.225×10^{-5}	1.681×10^{-8}	-8.164×10^{-12}	0.99621
S3	-0.03663	0.00434	-1.579 × 10 ⁻⁵	2.248×10^{-8}	-1.059×10^{-11}	0.83181
S4	-0.01741	5.832×10^{-4}	-1.705×10^{-7}	3.391×10^{-9}	-3.463×10^{-12}	0.99401
C1	-0.06711	0.00431	-1.422×10^{-5}	1.851×10^{-8}	-8.422×10^{-12}	0.89946
C2	-0.04196	0.00252	-4.357×10^{-6}	2.682×10^{-9}	-7.119×10^{-13}	0.96541

 $D_{\varepsilon,\mathrm{Max}}$ value. At this time, the D_{c}^T value of M0 was the largest, at 0.726, which was 79.8% of $D_{\varepsilon, \text{Max}}$, and higher than other MPC groups. The D_c^T values of F1-F4 were 0.647, 0.599, 0.679, and 0.714, respectively, which were 65.3, 59.9, 67.9, and 71.4% of $D_{\varepsilon,\text{Max}}$ and 10.9, 17.5, 6.5, and 1.7% lower than M0, respectively. The D_c^T values of S1–S4 were 0.310, 0.533, 0.408, and 0.571, which were 31.0, 55.0, 48.0, and 72.3% of $D_{\varepsilon,\text{Max}}$ and lower than that of M0 by 57.3, 26.6, 43.8, and 21.3%, respectively. The D_c^T values of C1 and C2 were 0.386 and 0.432, at 38.6 and 43.2% of $D_{\varepsilon,\mathrm{Max}}$ and 46.8 and 40.5% lower than that of M0, respectively. After 600°C, the D_c^T value of MPC co-mixed with FA and SF was lower than that of other MPC groups. At 1,000°C, the D_c^T values of C1 and C2 were 0.112 and 0.094, which were 38.6 and 43.2% of $D_{\rm EMax}$, and 20.0 and 16.7% of M0, respectively, indicating that the MPC co-mixed with FA and SF has better hightemperature resistance.

The relationship between the temperature damage variable $D_{\rm c}^T$ and the action temperature of MPC after being treated at different temperatures was obtained by fitting the $D_{\rm c}^T$ values of MPC with different ratios through nonlinear regression analysis, as shown in Figure 16. In the figure, $D_{\rm c}^T$ denotes the temperature damage variable of MPC after being treated at various temperatures, T represents the action temperature, and d_0 , d_1 , d_2 , d_3 , and d_4 refer to the model coefficients, respectively, as listed in Table 7.

5 Conclusion

The uniaxial compression properties of MPC modified by FA and SF at different temperatures were thoroughly investigated in this work. Through the experimental analysis, the following conclusions can be derived:

- 1) The compressive strength of MPC decreased to varying degrees at different temperatures. FA and SF can enhance the compressive strength of MPC at elevated temperatures, increasing it by 6.7–74.8% at 600°C and by 18.5–103.9% at 1,000°C. A tendency for the MPC peak to increase with the increase in temperature was detected, but it was not significant.
- 2) At 20°C, the deformation modulus of MPC was 10.37–12.75 GPa, and the deformation modulus of FA- and SF-modified MPC was lower than that of M0. By increasing the ambient temperature, the deformation modulus of MPC exhibited a trend of first decreasing and then increasing, and at 1,000°C, the deformation modulus of MPC was 5.09–10.92 GPa.
- 3) Through the nonlinear regression analysis, the model proposed in this work can better predict the compressive

strength, peak strain, and deformation modulus of FAand SF-modified MPC after being treated at different temperatures. Based on damage mechanics theory and the principle of equivalent stress, the axial compression damage constitutive model of MPC can better characterize the axial compression stress—strain relationship of FA- and SF-modified MPC after action at different temperatures. The correlation coefficient of the prediction model was greater than 0.97.

4) The MPC after being treated at different temperatures exhibited irreversible initial temperature damage, and the total damage variable D increased in an "S-shaped" trend under the action of axial compression loading. The temperature damage variable D_c^T first increased and then decreased by increasing the action temperature, and the rising section was mainly concentrated at $20-600^{\circ}$ C. At 600° C, the D_c^T value reached more than 30% of the total damage variable D corresponding to the peak strain, and at 1,000°C, and it was more than 10% of the total damage variable D corresponding to the peak strain. There exists a strong functional relationship between the D_c^T value and temperature.

Acknowledgments: This research work was supported by the National Natural Science Foundation Program of China (Grant No. 52168031), the Natural Science Foundation Program of Inner Mongolia (Grant Nos 2024MS05056 and 2022QN01007), Basic Scientific Research Expenses Program of Universities directly under Inner Mongolia Autonomous Region (Grant Nos JY20220152 and JY20220222), Inner Mongolia University of Technology Scientific Research Project (Grant No. BS201944).

Funding information: The National Natural Science Foundation Program of China (Grant No. 52168031), the Natural Science Foundation Program of Inner Mongolia (Grant Nos 2024MS05056 and 2022QN01007), Basic Scientific Research Expenses Program of Universities directly under Inner Mongolia Autonomous Region (Grant Nos JY20220152 and JY20220222), Inner Mongolia University of Technology Scientific Research Project (Grant No. BS201944).

Author contributions: All authors have accepted responsibility for the entire content of this manuscript and approved its submission.

Conflict of interest: The authors state no conflict of interest.

Data availability statement: All data generated or analysed during this study are included in this published article.

References

- Perez-Cortes, P., K. Cabrera-Luna, and J. I. Escalante-Garcia. Alkaliactivated limestone/metakaolin cements exposed to high temperatures: Structural changes. Cement and Concrete Composites, Vol. 122, 2021, id. 104147.
- Huang, Z. C., J. C. M. Ho, J. Cui, F. M. Ren, X. Cheng, and M. H. Lai. Improving the post-fire behaviour of steel slag coarse aggregate concrete by adding GGBFS. Journal of Building Engineering, Vol. 76, 2023, id. 107283.
- Iwama, K. and K. Maekawa. Modeling of carbonation, de-carbonation and re-carbonation processes of structural concrete subjected to high temperature heating. Cement and Concrete Composites, Vol. 129, 2022, id. 104493.
- Burciaga-Díaz, O. and J. I. Escalante-García. Comparative performance of alkali activated slag/metakaolin cement pastes exposed to high temperatures. Cement and Concrete Composites, Vol. 84, 2017, pp. 157-166.
- Kong, Y., P. Huang, Z. Gao, Y. Gao, and Z. Ren. Effect of plateau environment on properties of magnesium phosphate cement-based materials. Available at SSRN 4387431.
- Fang, B., Z. Hu, T. Shi, Y. Liu, X. Wang, D. Yang, et al. Research progress on the properties and applications of magnesium phosphate cement. Ceramics International, Vol. 49, 2023, pp. 4001-4016.
- Haque, M. A. and B. Chen. Research progresses on magnesium phosphate cement: A review. Construction and Building Materials, Vol. 211, 2019, pp. 885-898.
- Walling, S. A. and J. L. Provis. Magnesia-based cements: a journey of 150 years, and cements for the future? Chemical Reviews, Vol. 116, No. 7, 2016, pp. 4170-4204.
- Liu, J., Y. Yan, Z. Li, F. Yang, R. Hai, and M. Yuan. Investigation on the potassium magnesium phosphate cement modified by pretreated red mud: Basic properties, water resistance and hydration heat. Construction and Building Materials, Vol. 368, 2023, id. 130456.
- [10] Ma, C., G. Chen, Z. Jiang, H. Zhou, H. Yao, R. Zhou, et al. Rheological properties of magnesium phosphate cement with different M/P ratios. Construction and Building Materials, Vol. 282, 2021, id. 122657.
- [11] Wu, J., Z. Lai, Q. Deng, and M. Liu. Effects of various curing conditions on volume stability of magnesium phosphate cement. Advances in Materials Science and Engineering, Vol. 2021, 2021, pp. 1–12.
- [12] Liu, F., B. Pan, P. Cao, and C. Zhou. Multi-scale characterization on behaviors of the interface between magnesium phosphate cement and portland cement. Construction and Building Materials, Vol. 275, 2021, id. 122139.
- [13] Liu, F., B. Pan, and C. Zhou. Experimental study on a novel modified magnesium phosphate cement mortar used for rapid repair of portland cement concrete pavement in seasonally frozen areas. Journal of Materials in Civil Engineering, Vol. 34, No. 3, 2022, id. 04021483.
- [14] Haque, M. A. and B. Chen. In vitro and in vivo research advancements on the magnesium phosphate cement biomaterials: A review. Materialia, Vol. 13, 2020, id. 100852.
- [15] Zhang, Q., X. Cao, R. Ma, S. Sun, L. Fang, J. Lin, et al. Solid wastebased magnesium phosphate cements: Preparation, performance and solidification/stabilization mechanism. Construction and Building Materials, Vol. 297, 2021, id. 123761.
- Golewski, G. L. Examination of water absorption of low volume fly ash concrete (LVFAC) under water immersion conditions. Materials Research Express, Vol. 10, No. 8, 2023, id. 085505.

- [17] Golewski, G. L. The role of pozzolanic activity of siliceous fly ash in the formation of the structure of sustainable cementitious composites. Sustainable Chemistry, Vol. 3, No. 4, 2022, pp. 520-534.
- [18] Golewski, G. L. Study of strength and microstructure of a new sustainable concrete incorporating pozzolanic materials. Structural Engineering and Mechanics An Int'l Journal, Vol. 86, No. 4, 2023,
- Feng, W., Y. Tang, Y. Zhang, C. Qi, L. Ma, and L. Li. Partially fly ash [19] and nano-silica incorporated recycled coarse aggregate based concrete: Constitutive model and enhancement mechanism. Journal of Materials Research and Technology, Vol. 17, 2022, pp. 192-210.
- [20] Golewski, G. L. Investigating the effect of using three pozzolans (including the nanoadditive) in combination on the formation and development of cracks in concretes using non-contact measurement method. Advances in Nano Research, Vol. 16, No. 3, 2024, id. 217.
- [21] Golewski, G. L. Enhancement fracture behavior of sustainable cementitious composites using synergy between fly ash (FA) and nanosilica (NS) in the assessment based on digital image processing procedure. Theoretical and Applied Fracture Mechanics, Vol. 131, 2024, id. 104442.
- Golewski, G. L. Assessing of water absorption on concrete com-[22] posites containing fly ash up to 30% in regards to structures completely immersed in water. Case Studies in Construction Materials, Vol. 19, 2023, id. e02337.
- [23] Feng, H., S. Nie, A. Guo, L. Lv, and J. Yu. Evaluation on the performance of magnesium phosphate cement-based engineered cementitious composites (MPC-ECC) with blended fly ash/ silica fume. Construction and Building Materials, Vol. 341, 2022, id. 127861.
- [24] Dai, X., J. Qian, J. Qin, Y. Yue, Y. Zhao, and X. Jia. Preparation and properties of magnesium phosphate cement-based fire retardant coating for steel. Materials, Vol. 15, No. 12, 2022, id. 4134.
- [25] Dai, X., L. Lian, X. Jia, J. Qian, and J. Qin. Preparation and properties of magnesium phosphate cement with recycled magnesia from waste magnesia refractory bricks. Journal of Building Engineering, Vol. 63, 2023, id. 105491.
- [26] Li, Y., T. Shi, B. Chen, and Y. Li. Performance of magnesium phosphate cement at elevated temperatures. Construction and Building Materials, Vol. 91, 2015, pp. 126-132.
- [27] Dai, X., W. Ren, J. Qin, X. Jia, and J. Qian. Influence and mechanism of borax on the physico-mechanical properties of magnesium potassium phosphate cement exposed to high temperatures. Construction and Building Materials, Vol. 376, 2023, id. 131015.
- [28] Gardner, L. J., S. A. Walling, C. L. Corkhill, S. A. Bernal, V. Lejeune, M. C. Stennett, et al. Temperature transformation of blended magnesium potassium phosphate cement binders. Cement and Concrete Research, Vol. 141, 2021, id. 106332.
- Zhang, X., G. Li, M. Niu, and Z. Song. Effect of calcium aluminate cement on water resistance and high-temperature resistance of magnesium-potassium phosphate cement. Construction and Building Materials, Vol. 175, 2018, pp. 768-776.
- Fang, Y., P. Cui, Z. Ding, and J. X. Zhu. Properties of a magnesium phosphate cement-based fire-retardant coating containing glass fiber or glass fiber powder. Construction and Building Materials, Vol. 162, 2018, pp. 553-560.
- Yu, J., J. Qian, H. Chen, Y. Ji, D. Kuang, and X. Jia. Thermal behavior of magnesium phosphate cement with addition of sulphoaluminate cement. Available at SSRN 4444376.

22

- [32] Dong, D., Y. Huang, Y. Pei, X. Zhang, N. Cui, P. Zhao, et al. Effect of spherical silica fume and fly ash on the rheological property, fluidity, setting time, compressive strength, water resistance and drying shrinkage of magnesium ammonium phosphate cement. *Journal of Building Engineering*, Vol. 63, 2023, id. 105484.
- [33] Feng, H., J. Liang, A. Guo, L. Lv, Z. Sun, M. N. Sheikh, et al. Development and design of ultra-high ductile magnesium phosphate cement-based composite using fly ash and silica fume. Cement and Concrete Composites, Vol. 137, 2023, id. 104923.
- [34] Xu, B., H. Ma, H. Shao, Z. Li, and B. Lothenbach. Influence of fly ash on compressive strength and micro-characteristics of magnesium potassium phosphate cement mortars. *Cement and Concrete Research*, Vol. 99, 2017, pp. 86–94.
- [35] Runqing, L., W. Wei, Q. Dingwen, and Y. Yuanquan. Static and dynamic mechanical properties of magnesium phosphate cement modified by metakaolin after high-temperature treatment. *Construction and Building Materials*, Vol. 392, 2023, id. 131933.
- [36] Guo, W., S. Wang, Z. Xu, Z. Zhang, C. Zhang, Y. Bai, et al. Mechanical performance and microstructure improvement of soda residue–carbide slag–ground granulated blast furnace slag binder by optimizing its preparation process and curing method. *Construction and Building Materials*, Vol. 302, 2021, id. 124403.

- [37] Lemaitre, J. How to use damage mechanics. Nuclear Engineering and Design, Vol. 80, No. 2, 1984, pp. 233–245.
- [38] Shen, M., J. Bi, Y. Zhao, C. Wang, T. Wei, and B. Du. Study on the mechanical characteristics and damage evaluation of concrete-rock combination after high temperatures exposure. *Construction and Building Materials*, Vol. 330, 2022, id. 127278.
- [39] Wu, Q., Q. Ma, and J. Zhang. Mechanical properties and damage constitutive model of concrete under low-temperature action. *Construction and Building Materials*, Vol. 348, 2022, id. 128668.
- [40] Zhang, Y., Z. Ma, X. Zhi, X. Chen, J. Zhou, L. Wei, et al. Damage characteristics and constitutive model of phosphogypsum/fly ash/ slag recycled aggregate concrete under uniaxial compression. *Cement and Concrete Composites*, Vol. 138, 2023, id. 104980.
- [41] Wang, L., Y. Zhao, and Y. Xing. Investigating high-temperature deformation evolution of concrete under sustained loading using DIC technology and a temperature-mechanical coupled damage constitutive model. *Construction and Building Materials*, Vol. 324, 2022, id. 126638.
- [42] Pan J., Y. Zhang, P. Li, X. Wu, and X. Xi. Mechanical properties and thermo-chemical damage constitutive model of granite subjected to thermal and chemical treatments under uniaxial compression. *Construction and Building Materials*, Vol. 390, 2023, id. 131755.